Impact of Geometric Variability on Compressor Repeating-Stage Performance

by

Antoine Vincent

Diplôme d'ingénieur, École Polytechnique, Palaiseau (2002)

Submitted to the Department of Aeronautics and Astronautics
in partial fulfillment of the requirements for the degree of

Master of Science in Aeronautics and Astronautics

at the

MASSACHUSETTS INSTITUTE OF TECHNOLOGY

September 2003

© Antoine Vincent, MMIII. All rights reserved.

The author hereby grants to MIT permission to reproduce and distribute publicly
paper and electronic copies of this thesis document in whole or in part.

Author .....
Department of Aeronautics and Astronautics
August 22, 2003

Certified by .....
Edward M. Greitzer
H.N. Slater Professor of Aeronautics and Astronautics
Thesis Supervisor

Accepted by .....
Edward M. Greitzer
H.N. Slater Professor of Aeronautics and Astronautics
Chair, Committee on Graduate Students

Impact of Geometric Variability on Compressor Repeating-Stage Performance

by

Antoine Vincent

Submitted to the Department of Aeronautics and Astronautics
on August 22, 2003, in partial fulfillment of the
requirements for the degree of
Master of Science in Aeronautics and Astronautics

Abstract

The impact of geometric variability on compressor performance is investigated using a compressor repeating-stage model based on well-known correlations for profile losses, end-wall blockage, deviation, and the onset of stall. Previous computations with a quasi-two-dimensional cascade analysis code are used to link geometric variability to performance deviations. Performance variability is then introduced probabilistically through random perturbations to tip clearances, profile losses and turning. For the variation input, at design incidence, the mean efficiency is found to decrease by 1%, mostly due to the mean shift in profile losses, and the mean pressure rise is reduced by 2.5%, mostly because of the mean shift in turning. A parametric study for compressor stages of different designs shows a lower degradation of mean performance and a lower performance variability for stages which have higher work coefficient, lower degree of reaction, and higher blade aspect ratio.

It was found that the influence of blade profile effects was well represented, but the impact of tip clearance variation was not well captured when compared to three-dimensional computations. It is concluded that to address the effects of tip clearance variability, emphasis should be placed on development of models which both can include the alteration of end-wall displacement thickness within the compressor stage and are appropriate for probabilistic description.

Thesis Supervisor: Edward M. Greitzer
Title: H.N. Slater Professor of Aeronautics and Astronautics

Acknowledgments

The author is indebted for his guidance and encouragements to Professor Edward M. Greitzer, who proposed the subject of this thesis and served as his advisor. The support of Professor David L. Darmofal and the suggestions of M. V. Casey of Sulzer Innotec were also appreciated. Many students, faculty and staff members of the MIT Gas Turbine Laboratory contributed to the present work through their lectures, suggestions and technical support.

Among them, Jérome Lavainne, Vincent Perrot and Josep Dorca-Luque spent several days in the validation the compressor algorithm, their help had to be acknowledged. The availability of Doctor Victor E. Garzon was also very precious: he suggested the details of the probabilistic approach, and several parts of this thesis are based on his algorithms.

The author would like to thank his office colleagues Borislav Sirakov, Nathan Fitzgerald and Vai–Man Lei for their support, Johnny Giraldo and Kelly Silfies for their salsa class, and Jason LaPenta for serving as unofficial head of the MIT underwater hockey club.

This section would not be complete if it did not mention Remo Ziegler, coach of the MIT handball team, and Victor Martinez de Albeniz, its founding president. Thanks to their year long dedication, the New England Freezes won the gold medal in the US nationals last April.

This work was made possible by the financial support of the French defense procurement agency *Délégation Générale pour l'Armement*. The assistance provided during the last two years by Olivier Etchevers, deputy head of the Aircraft Engine Group, was especially appreciated.

Contents

1 Introduction **11**
- 1.1 Background and Motivation . . . 11
- 1.2 Objectives . . . 11
- 1.3 Contributions . . . 12

2 Literature Survey **13**
- 2.1 Compressor Repeating-Stage . . . 13
- 2.2 Profile Losses . . . 13
- 2.3 Deviation . . . 13
- 2.4 End-Wall Losses . . . 13
- 2.5 Stalling Static Pressure Rise . . . 14
- 2.6 Geometric Variability . . . 14
- 2.7 Mean-Line Analysis of the Geometric Variations . . . 17
- 2.8 Three-Dimensional Analysis of the Geometric Variations . . . 19

3 Compressor Repeating-Stage Algorithm **20**
- 3.1 Hypotheses . . . 20
- 3.2 Compressor Geometry . . . 21
  - 3.2.1 Overall Stage Geometry . . . 21
  - 3.2.2 Blade Row Geometry . . . 21
  - 3.2.3 Air Angle and Velocity Vector Geometry . . . 22
- 3.3 End-Wall Model . . . 23
- 3.4 Layout of the Algorithm . . . 25
  - 3.4.1 Algorithm Input . . . 25
  - 3.4.2 Algorithm Steps . . . 25
- 3.5 Program Output and Validation . . . 26

4 Analysis of Sensitivity to Geometric Variability **29**
- 4.1 Characterization of Geometric Variability . . . 29
  - 4.1.1 Definitions for the Probabilistic Analysis . . . 29
  - 4.1.2 Selection of Geometric Parameters . . . 30
  - 4.1.3 Model for Tip Clearance Variability . . . 30
  - 4.1.4 Blade Profile Variability . . . 31
  - 4.1.5 Model for Blade Profile Variability . . . 33
- 4.2 Implementation of Variability in the Algorithm . . . 34
  - 4.2.1 Equations . . . 34
  - 4.2.2 Interdependence of Variables . . . 34

4.2.3 Probabilistic Input . . . 35
4.3 Performance Results . . . 35
4.3.1 Sensitivity to Individual Parameters . . . 35
4.3.2 Baseline Monte Carlo Simulation . . . 38
4.3.3 Relative Importance of Sources of Variability . . . 38
4.3.4 Variation of Mean Shift Factor . . . 42
4.3.5 Sensitivity of Different Compressor Designs to Geometric Variability 44
4.3.6 Variation of Blade Aspect Ratio . . . 44
4.4 Comparison With Other Information About Variability . . . 44
4.4.1 The One-Dimensional Model of Garzon . . . 44
4.4.2 The Mean-Line Model of Lavainne . . . 47
4.4.3 The Three-Dimensional Model of Lavainne . . . 49

5 Summary and Recommendations 50
5.1 Summary . . . 50
5.2 Suggestions for Future Work . . . 51

A Repeating-Stage Implementation 52
A.1 Overall View . . . 52
A.2 Initialization Tasks . . . 52
A.2.1 Program Input and First Geometric Parameters . . . 52
A.2.2 Reference Deviation and Incidence Angles . . . 55
A.2.3 From Metal Angles to Design Coefficients . . . 55
A.2.4 From Design Coefficients to Metal Angles . . . 56
A.2.5 Other Fixed Parameters . . . 56
A.2.6 Expression of Inlet Conditions as Input Coefficients . . . 57
A.3 Main Program Loop . . . 57
A.3.1 Flow Chart . . . 57
A.3.2 Resolution of Velocity Triangles . . . 59
A.3.3 Profile Losses . . . 60
A.3.4 End-Wall Losses . . . 61
A.3.5 Stalling Static Pressure Rise Coefficient and Stage Loading Ratio . . 62
A.4 Determination of Characteristic Points . . . 63
A.4.1 Surge Point . . . 63
A.4.2 Choke Point . . . 65
A.5 Output Files . . . 65
A.5.1 OUTPUT.TXT . . . 65
A.5.2 OUTPUT2.TXT . . . 68

B Probabilistic Analysis Implementation 70
B.1 Overall View . . . 70
B.2 Monte Carlo Simulation . . . 71
B.2.1 Introduction of Geometric Variability . . . 71
B.2.2 Baseline Simulation . . . 72
B.2.3 Implementation of Variability in CHARAX . . . 73
B.3 Statistics for All the Stages . . . 73

List of Figures

2-1 Example of profile losses computed from the correlations of Lieblein [13] . . 14
2-2 Displacement thickness, δ^*, and tangential force thickness, τ, vs. stage loading ratio Ω, for a given ratio of tip clearance to airfoil trailing-edge staggered spacing $\frac{\epsilon}{g}$ [11] 15
2-3 Correlation of maximum stall pressure rise, taken from Koch [10] 15
2-4 Rotor losses and turning angle vs. incidence. Comparison between the nominal design and the mean performance of a Monte Carlo simulation (MCS) for the IBR rotor studied by Garzon [6]. $\hat{\mu}$ represents mean values, $\hat{\sigma}$ represents standard deviations. 16

3-1 Cross-section of an axial compressor stage 21
3-2 Blade row geometry 22
3-3 Stage velocity triangles 23
3-4 Geometry for incidence and deviation angles 24
3-5 Stage characteristic constructed from free-stream performance and end-wall boundary layer [16] 24
3-6 Characteristic curves for the INDUS compressor 27
3-7 Pressure rise and efficiency when stator vanes are restaggered in steps of 5 degrees for the INDUS compressor 28

4-1 Probabilistic distribution of the ratio of tip clearance to blade height for the INDUS compressor 30
4-2 Normalized rotor losses and turning angle vs. incidence. Mean shift and coefficient of variability obtained by Garzon for the IBR rotor [6] 32
4-3 Probabilistic distribution of the input parameters for the Monte Carlo simulation. "MCS" is the Monte Carlo simulation for the INDUS compressor. "Garzon" is the Monte Carlo simulation for the IBR rotor as reported by Garzon [6]. "Shift" is the deterministic simulation of the INDUS compressor where only mean shift is accounted for. 36
4-4 Probabilistic results for pressure rise and efficiency. "MCS" is the Monte Carlo simulation for the INDUS compressor. "Shift" is the deterministic simulation of the INDUS compressor where only mean shift is accounted for. 39
4-5 Mean shift for different sources of variability for the INDUS compressor. ϵ is the variability of tip clearance, ω is the variability of the losses, ϑ is the variability of the turning. 40
4-6 Coefficient of variability (COV) for different sources of variability for the INDUS compressor. ϵ is the variability of tip clearance, ω is the variability of the losses, ϑ is the variability of the turning. 41

4-7 Performance dependence on the mean shift factor for the INDUS compressor at design incidence. Pressure rise and efficiency are calculated using Monte Carlo simulation, and compared through their mean shift, coefficient of variability (COV) and skewness. 43
4-8 Performance of variants of the INDUS compressor, computed using Monte Carlo simulation at design incidence. Compressors differ in work coefficient $\frac{C_{u2}-C_{u1}}{U}$ and degree of reaction R. 45
4-9 Performance of variants of the INDUS compressor, computed using Monte Carlo simulation at design incidence. Compressors differ in blade aspect ratio A_{rat}. Physical tip clearances and blade profiles are maintained the same. . 46

A-1 Algorithm flow diagram 53
A-2 Curve module 58
A-3 Velocity triangle resolution module 59
A-4 Surge module 64
A-5 Choke module 66

B-1 Flow diagram for the probabilistic analysis 71

List of Tables

2.1 Mean shift and standard deviation of the Monte Carlo analysis on the response surface of the mean-line sensitivity analysis at design incidence, using the quasi-3D algorithm of Lavainne with the third stage of the CREATE compressor (from Tables 4.2 and 4.3 in [12]). $*$ represents nominal values in absence of variability. The ratio of the stagnation pressures is given by $\pi = \frac{p_{T3}}{p_{T1}}$. 18

4.1 Interdependence of variables 34

4.2 Deterministic sensitivity analysis for the INDUS compressor at design incidence by assigning geometric parameters to their $\pm 2\sigma$ values 35

4.3 Mean shift and coefficient of variability of the Monte Carlo analysis at design incidence for the INDUS compressor 42

4.4 Statistical results of the Monte Carlo analysis using the mean-line algorithm of Garzon on the STAGE1 compressor at design incidence. Figures in parentheses correspond to the INDUS compressor analyzed with the mean-line method developed in this thesis. 47

4.5 Mean shift and variability of the Monte Carlo analysis on the response surface of the sensitivity analysis at design incidence, using the mean-line algorithm of Lavainne with the third stage of the CREATE compressor [12]. 48

4.6 Mean shift and variability of the Monte Carlo analysis at design incidence, using the model detailed in this thesis with the INDUS compressor. 48

4.7 Mean shift and variability of the Monte Carlo analysis on the response surface of the sensitivity analysis at design incidence, using the 3D algorithm of Lavainne with the third stage of the CREATE compressor [12]. 49

Nomenclature

Roman

A_{rat}	blade aspect ratio
C	air absolute velocity
c	blade chord length
C_p	static pressure rise coefficient
C_u	air circumferential velocity
C_x	air axial velocity
D	casing hub diameter
g	staggered spacing between blades
h	compressor annulus height
i	air incidence angle
i_n	reduced air incidence angle
L	arc–length of airfoil
M_a	Mach number
N	number of blades or vanes
p	static pressure
p_T	stagnation pressure
R	degree of reaction
R_b	ideal gas constant
r	radius
R_a	center-line average roughness
R_e	Reynolds number
$\hat{S}$	mean shift of a random variable
s	blade circumferential spacing
$\hat{SK}$	skewness of a random variable
T	temperature
t	blade maximum thickness
U	blade speed at the r.m.s. radius
$\hat{V}$	coefficient of variability of a random variable
W	air relative velocity

Greek

α	rotor absolute air angle
β	rotor relative air angle
$\Gamma^{\hat{S}}$	mean shift factor
$\Gamma^{\hat{V}}$	coefficient of variability factor
γ	polytropic coefficient

δ	air deviation angle
δ^*	boundary layer displacement thickness
δ_x	axial spacing between blade rows
ϵ	blade tip clearance
λ	r.m.s. radius factor
η	stage efficiency
θ'	blade stagger angle
ϑ	air turning angle
μ	air dynamic viscosity
$\hat{\mu}$	mean value of a random variable
μ_y	hub stage pressure coefficient
ν	hub flow coefficient
π	stage pressure ratio
σ	blade solidity
$\hat{\sigma}$	standard deviation of a random variable
τ	boundary layer tangential-force thickness
ϕ'	blade camber angle
ϕ	flow coefficient at the r.m.s. radius
Ω	stage loading ratio
ρ	air density
ω	total pressure loss coefficient

Subscripts

$()_h$	casing hub
$()_t$	casing tip
$()_{pro}$	profile values, without end-wall
$()_r$	rotor
$()_s$	stator
$()_1$	rotor inlet position
$()_2$	rotor outlet position
$()_3$	stator outlet position

Superscripts

$()'$	blade values
$()^*$	design values

Acronyms

COV	Coefficient Of Variability
IBR	Integrally Bladed Rotor
MCS	Monte Carlo Simulation
PCA	Principal Component Analysis
r.m.s.	Root Mean Squared

Chapter 1

Introduction

1.1 Background and Motivation

Decreasing the impact of geometric variability on compressor performance is one factor that can contribute to turbine engine affordability. Variability has been shown to lead to drops in compressor efficiency and corollary increases in specific fuel consumption of the order of 1% [6]. Because fuel can represent 30% of the direct operating costs [9], these drops are important to the users. Geometric variability can occur through wear, especially leading-edge erosion and corrosion. It can also occur through imprecision in the manufacturing of the blades themselves.

Although the detrimental impact of geometric variability of the blade profiles on compressor performance is acknowledged, only limited quantitative information on this effect can be found in the open literature. Garzon [6] carried out a quasi-2D analysis to compute the impact on the compressor aerodynamic performance of representative geometric variations. Based on this work, correlations of loss and turning were also introduced in a mean-line multistage compressor analysis to estimate the influence on overall performance.

Garzon suggested that it was important to account for the effects of casing boundary layer blockage and tip clearance variability. This work is an initial step in the approach to this problem using a mean-line repeating-stage analysis.

1.2 Objectives

Objectives of the work reported in this thesis are:

- Implementation of a mean-line repeating-stage algorithm for assessing axial compressor aerodynamic performance, including end-wall blockage.
- Linking this algorithm to a model of geometric variability, examination of the effects of variability on compressor performance, in terms of pressure rise and efficiency.
- Determination and ranking of the geometric parameters that have a major impact on compressor performance mean shift and variability.

1.3 Contributions

Following a model developed by Casey [1], a mean-line algorithm has been built to assess the performance of axial compressors. Largely based on data available in the open literature, the model includes correlations for incidence, deviation, profile losses, end-wall and stalling static pressure rise. This algorithm has been tested and validated at Mach numbers typical of industrial compressors.

Following Garzon [6], geometric variability is incorporated into the analysis as a probabilistic perturbation of turning angle and profile losses. Monte Carlo simulations allow a probabilistic assessment of the impact of geometric variability on a stage. The relative importance of different sources of variability has been investigated. The relative sensitivity to geometric variability of variants of a compressor stage differing in degree of reaction and work coefficient has been studied. This sensitivity has also been investigated for compressors differing in blade aspect ratio. Mean shift and variability results have been compared with the one-dimensional algorithm of Garzon [6], the mean-line quasi-three-dimensional, and the three-dimensional algorithms of Lavainne [12].

Chapter 2

Literature Survey

2.1 Compressor Repeating-Stage

Casey [1, 2] developed a method to compute the performance of an axial compressor repeating-stage. This one-dimensional analysis plus a suite of correlations for losses, deviations and end-wall effects account for all main features of stage performance at pressure ratios characteristic of industrial compressors ($\pi < 1.2$). Three classes of effects are addressed and will be detailed in the subsequent sections:

1. cascade aerodynamics, through profile losses and deviation angle as a function of incidence;
2. casing and hub boundary layers (clearance losses, loss in work capability and end-wall blockage as a function of tip clearance and stage loading);
3. the onset of rotating stall.

The correlations used are well-known and will thus be described only briefly.

2.2 Profile Losses

Lieblein [13] compiled data from two-dimensional cascade experiments to estimate profile losses. A typical example of the application of the correlations can be found in Figure 2-1. These results have been modified to account for differences in Reynolds and Mach numbers, incidence angle, blade roughness and chord length [8, 11].

2.3 Deviation

Lieblein [14] compiled data from two-dimensional cascade experiments and proposed a method to compute the deviation of the flow angles from the blade metal angles. Based on the further results of Crouse [3] and Davis [4], the iterative procedure that yields reference values for deviation and incidence angles is detailed in Section A.2.2.

2.4 End-Wall Losses

Koch and Smith [11] developed a model for end-wall losses at the compressor hub and tip. There are two physical processes to be addressed. For a given pressure rise, end-wall

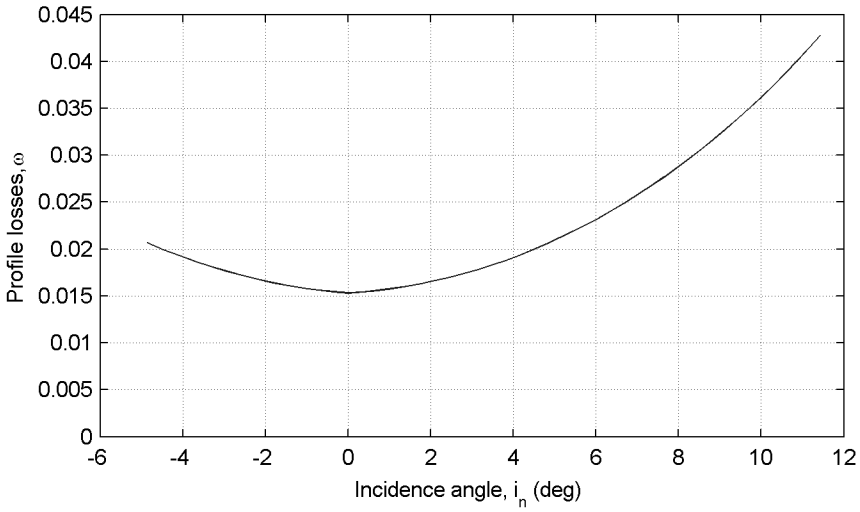

Figure 2-1: Example of profile losses computed from the correlations of Lieblein [13]

boundary layers cause a mass flow deficit that can be characterized by the displacement thickness δ^*. The blockage increases with tip clearance and with the ratio of stage loading to maximum stage loading. The blockage is associated with a loss and hence a reduction in efficiency. However, there is also a deficit in tangential blade force in the end-wall region because of the clearance boundary layer. The input torque is lower than if the blade extended all the way to the wall. Koch and Smith provided correlations to compute the quantities δ^* and τ (the so-called tangential force thickness, which is a measure of the force deficit) in terms of tip clearance and stage loading ratio, as depicted in Figure 2-2.

2.5 Stalling Static Pressure Rise

Koch [10] presented data from single and multistage compressors showing the dependence of stalling static pressure rise coefficient on the ratio of airfoil arc-length L to airfoil trailing-edge staggered spacing g. The analogy given is based on the idea that a passage in a blade row behaves like a two-dimensional diffuser: the arc-length corresponds to the diffuser length, and the staggered spacing to the diffuser width. A correlation for two-dimensional diffusers is shown in Figure 2-3, compared with single and multistage compressor data [10]. Corrective factors are added for Reynolds number, blade tip clearance, blade row axial spacing and effective inlet dynamic pressure. This last addresses the effects of vector diagram type, inlet skew and boundary layers. Koch showed that stalling pressure rise data at or near design speed for high speed compressors was consistent with these low-speed correlations.

2.6 Geometric Variability

Garzon [6] used statistical and probabilistic techniques to assess the impact of geometric variability on axial compressor performance. He used principal component analysis (PCA) to analyze a set of high-resolution compressor blade surface measurements. PCA consists in finding a statistically optimal basis for representing the scatter of the measured data. PCA

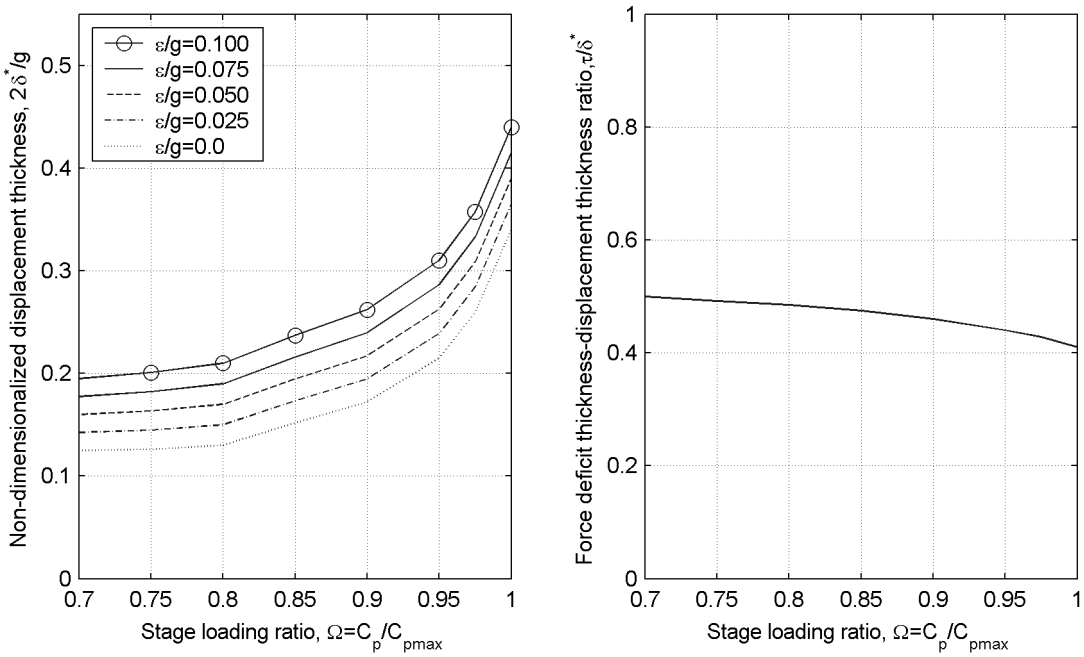

Figure 2-2: Displacement thickness, δ^*, and tangential force thickness, τ, vs. stage loading ratio Ω, for a given ratio of tip clearance to airfoil trailing-edge staggered spacing $\frac{\epsilon}{g}$ [11]

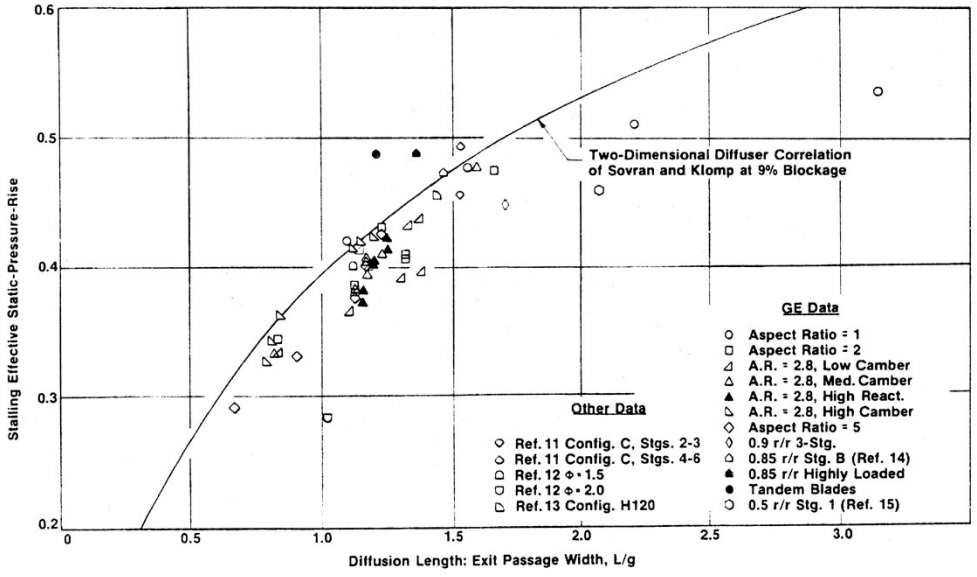

Figure 2-3: Correlation of maximum stall pressure rise, taken from Koch [10]

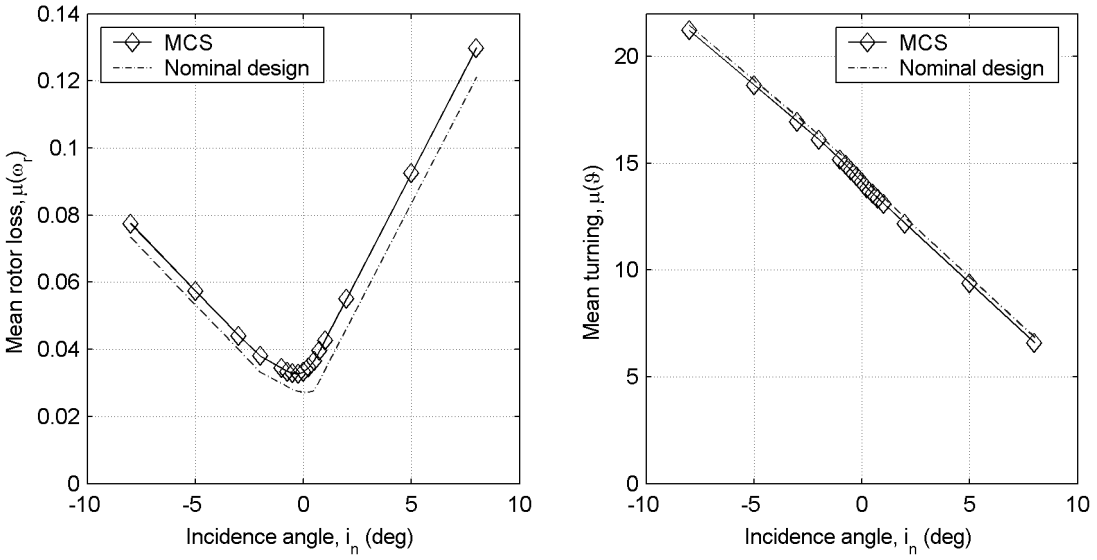

(a)

(b)

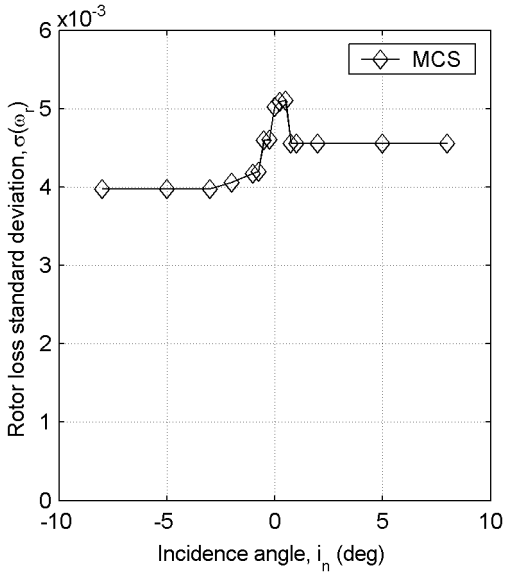

(c)

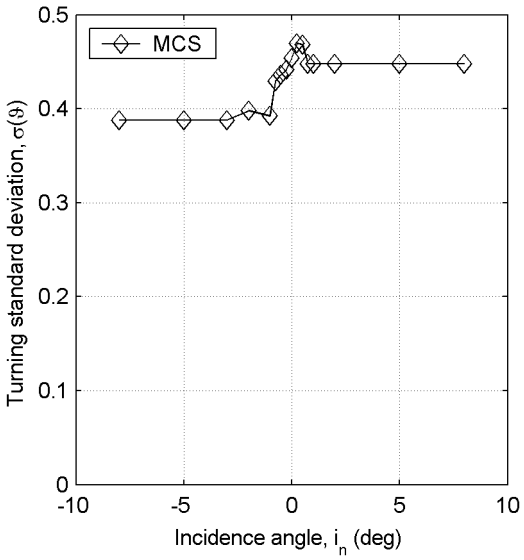

(d)

Figure 2-4: Rotor losses and turning angle vs. incidence. Comparison between the nominal design and the mean performance of a Monte Carlo simulation (MCS) for the IBR rotor studied by Garzon [6]. $\hat{\mu}$ represents mean values, $\hat{\sigma}$ represents standard deviations.

can be shown to be equivalent to singular value decomposition [17]. The analysis resulted in high-fidelity models of geometric variability due to manufacturing. The impact of this variability on blade row aerodynamic performance was then assessed using a Monte Carlo simulation (MCS) and the quasi two-dimensional cascade analysis code MISES, written by Drela [5].

Results for an integrally bladed rotor (IBR) are presented in Figure 2-4. The effects of geometric variability are represented in terms of profile losses ω_r and turning ϑ. On the graphs, the nominal condition is compared to the mean performance of the probabilistic geometry corresponding to the Monte Carlo simulations. Geometric variability causes a 23% increase in profile losses, and a 2% decrease in turning. The standard deviations for rotor losses and turning in Figures 2-4c and 2-4d remain relatively constant for different incidence angle.

Garzon carried out successful Monte Carlo simulations in the $[-4, 1]$ incidence angle range. Outside that range, the convergence rate of simulations dropped below 80%. Garzon extended the results to the $[-8, 8]$ range using linear interpolation. The flat segments for $i_n \leq -4deg$ and $i_n \geq 1deg$ in Figures 2-4c and 2-4d can therefore not be compared with the peaks appearing in the $[-4, 1]$ range. The origin of these peaks is still unclear, and may be related to the noise in the Monte Carlo simulation.

Garzon used the data presented in Figure 2-4 to build non-dimensionalized probabilistic models of loss coefficient and turning versus incidence. He incorporated them in a one-dimensional compressor model to assess the impact of geometric variability on overall performance. For a six stage compressor, with the input variability that he used, he found the difference between nominal and mean polytropic efficiency to be about one percentage point.

2.7 Mean-Line Analysis of the Geometric Variations

Lavainne [12] modelled blade profile variability using 2σ values from an industrial statistical sample. The variables were tip clearance, chord, leading and trailing edge angle and thickness, and maximum thickness. He conducted a deterministic sensitivity analysis of the third stage of the SNECMA Moteurs CREATE compressor, using a mean-line quasi-3D model associating MISES [5] with a model for end-wall flow blockage and losses. The end-wall correlations were an extension of the approach of Smith [16] to account for the significant increase in flow blockage across the rotor and the decrease in the stator. That effect is not included in the basic repeating-stage model developed in this thesis.

A quadratic response surface of the performance in pressure rise and efficiency was built and used to run a probabilistic analysis based on Monte Carlo simulations. Table 2.1 taken from [12] presents the mean shift and standard deviation of pressure ratio π and efficiency η when all geometric variability parameters are taken into account, and when they are removed one at a time. Lavainne observed a standard deviation in efficiency of one percentage point. He reported a 0.5% decrease in mean efficiency. He found that the main factors of performance mean shift were rotor leading edge angle thickness, and that the main factors of performance variability were rotor tip clearance and rotor leading edge angle.

Geometric parameter	$100 \cdot (\hat{\mu}_\pi - \pi^*)$	$100 \cdot (\hat{\mu}_\eta - \eta^*)$	$100 \cdot \hat{\sigma}_\pi$	$100 \cdot \hat{\sigma}_\eta$
All applied	-0.360	-0.590	0.968	1.156
Var. NOT applied	$100 \cdot (\hat{\mu}_{\pi_i} - \hat{\mu}_\pi)$	$100 \cdot (\hat{\mu}_{\eta_i} - \hat{\mu}_\eta)$	$100 \cdot (\hat{\sigma}_{\pi_i} - \hat{\sigma}_\pi)$	$100 \cdot (\hat{\sigma}_{\eta_i} - \hat{\sigma}_\eta)$
Rotor tip clearance ϵ_r	0.000	0.020	-0.112	-0.208
Stator tip clearance ϵ_s	0.019	0.044	-0.028	-0.146
Tip clearances ϵ_r, ϵ_s	0.023	0.058	-0.152	-0.390
Rotor chord c_r	0.000	0.022	-0.001	-0.001
Stator chord c_s	0.003	0.009	0.001	-0.001
Rotor LE Angle	0.179	0.208	-0.293	-0.129
Stator LE Angle	0.004	0.017	0.001	-0.001
Rotor TE Angle	-0.003	0.041	-0.016	-0.081
Stator TE Angle	0.004	0.008	0.001	-0.002
Rotor LE Thickness	0.111	0.109	-0.012	-0.011
Stator LE Thickness	0.000	0.028	0.000	-0.001
Rotor TE Thickness	0.010	0.006	0.000	-0.010
Stator TE Thickness	0.004	0.007	0.000	-0.001
Rotor Max. Thick. t_r	0.030	0.088	-0.068	-0.013
Stator Max. Thick t_s	0.006	0.021	0.000	-0.012

Table 2.1: Mean shift and standard deviation of the Monte Carlo analysis on the response surface of the mean-line sensitivity analysis at design incidence, using the quasi-3D algorithm of Lavainne with the third stage of the CREATE compressor (from Tables 4.2 and 4.3 in [12]). $*$ represents nominal values in absence of variability. The ratio of the stagnation pressures is given by $\pi = \frac{p_{T3}}{p_{T1}}$.

2.8 Three-Dimensional Analysis of the Geometric Variations

Lavainne [12] also carried out a sensitivity analysis using the three-dimensional Reynolds Average Navier-Stokes solver FINE/TURBO developed by NUMECA [15]. The deterministic analysis using the 3D simulation found a sensitivity of stage mean performance to rotor tip clearance four times larger than the analysis using the mean-line model of Lavainne. The probabilistic analysis using the 3D simulation attributed 60% of the mean decrease in stage pressure ratio and efficiency to rotor tip clearance, while the same analysis using the mean-line model found the mean effects of rotor tip clearance to be negligible. In a similar manner, the probabilistic 3D analysis attributed 75% of the performance variability to rotor tip clearance, while the mean-line model found less than 10%. To account for these differences, Lavainne conducted a probabilistic comparison of the 3D and mean-line models. The performance prediction difference was found to have a large variability which was mainly driven by the rotor tip clearance variability.

Chapter 3

Compressor Repeating-Stage Algorithm

3.1 Hypotheses

In this chapter, a mean-line algorithm is introduced to assess the performance of an axial compressor repeating-stage. This algorithm follows the method originally developed by Casey [1]. Details of the implementation can be found in Appendix A.

Correlations mentioned in the literature survey are used to compute:

- profile losses;
- deviation angles;
- end-wall blockage;
- onset of stall.

The main assumptions are:

1. A single repeating-stage in a multistage compressor is considered. Effects of stage matching are not taken into account.
2. The flow is one-dimensional, and values at the root mean squared (r.m.s.) radius are assumed to represent the whole stage annulus.
3. The repeating-stage has meridional velocity and flow angles at the outlet of the stage identical to those at the inlet.
4. There is a constant mean radius.
5. No annulus height variation is considered, although it would be necessary to converge annulus walls to account for the density increase and support the repeating-stage hypothesis.
6. The flow is subsonic.
7. Classical blade profile families are used for the correlations, comprising NACA 65-series and British C-series blades on circular arc camber lines.
8. Stall occurs when the static effective pressure rise C_p reaches the maximum value $C_{p_{max}}$ known from the correlations of Koch [10].

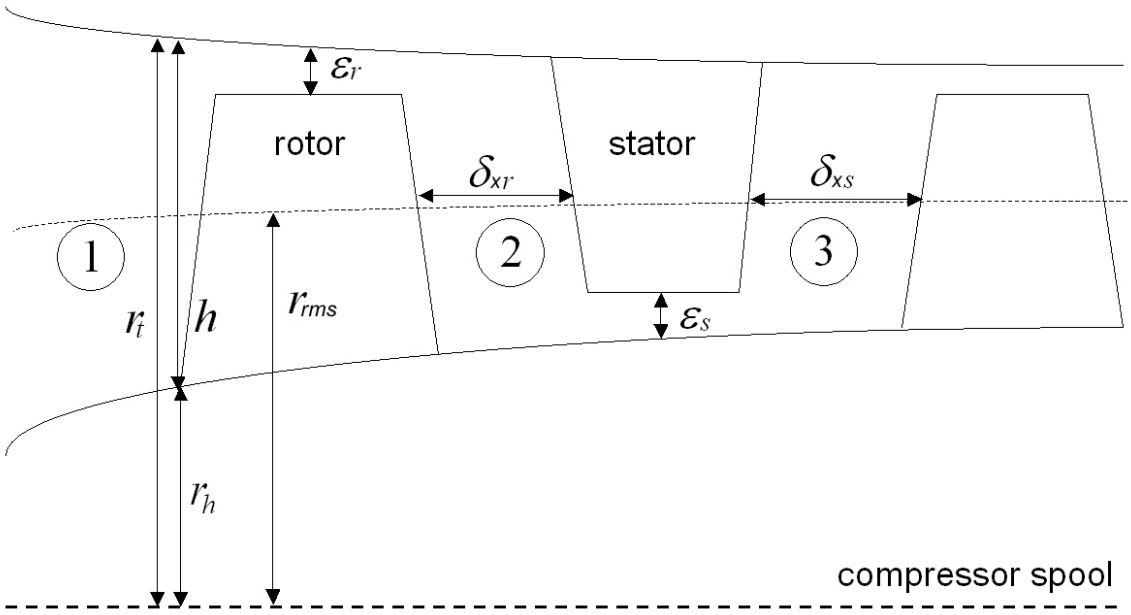

Figure 3-1: Cross-section of an axial compressor stage

3.2 Compressor Geometry

3.2.1 Overall Stage Geometry

Figure 3-1 exhibits the geometric layout of an axial compressor stage. The stage radii are determined by the hub radius r_h and the tip radius r_t. D is the hub diameter. h represents the blade annulus height, while ϵ_r and ϵ_s correspond respectively to the rotor and stator tip clearances. δ_{xr} and δ_{xs} are the rotor and stator axial spacing. Station ① corresponds to the rotor inlet, station ② corresponds to the stator inlet, while station ③ refers to the stator outlet. The r.m.s. radius r_{rms} is computed as follows:

$$r_{rms} = r_h \sqrt{\frac{\left(\frac{r_t}{r_h}\right)^2 + 1}{2}}.$$

3.2.2 Blade Row Geometry

The blade and vane profiles are characterized at the r.m.s. close up radius, r_{rms}, as illustrated in Figure 3-2. The blade profile maximum thickness is denoted by t, the chord length by c. R_a is the center-line average roughness parameter, which depends on the blade surface smoothness. From the number of blades N, the circumferential spacing, s, is given by:

$$s = \frac{2\pi r_{rms}}{N}.$$

The cascade solidity is defined as:

$$\sigma = \frac{c}{s}.$$

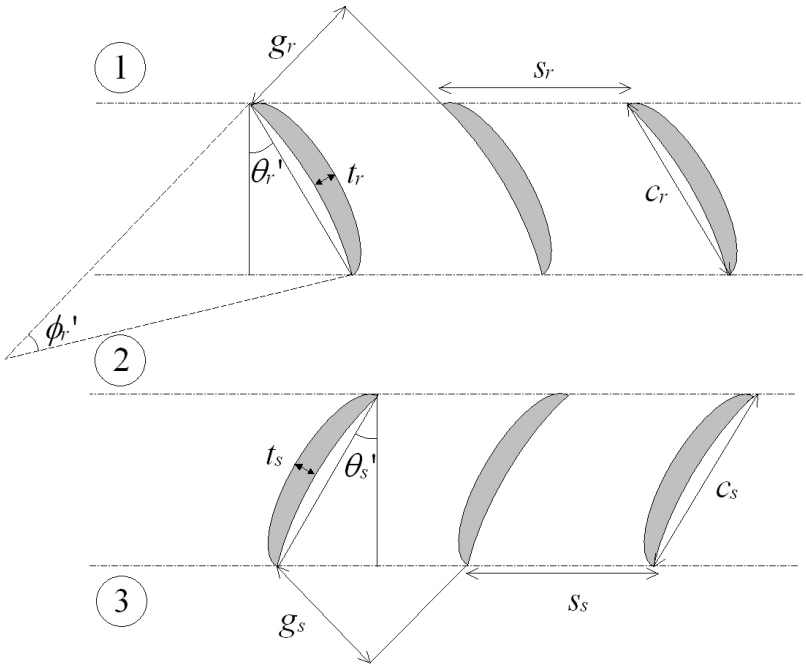

Figure 3-2: Blade row geometry

The airfoil stagger and camber angles are denoted respectively as θ' and ϕ'. The stagger and camber are linked to the rotor relative inlet and outlet metal angles ${\alpha_1}'$ and ${\alpha_2}'$, or to the rotor absolute inlet and outlet metal angles ${\beta_1}'$ and ${\beta_2}'$ through the relationships:

$$\begin{cases} {\phi'}_r = {\beta_1}' - {\beta_2}' \\ {\phi'}_s = {\alpha_2}' - {\alpha_1}' \\ {\theta'}_r = \frac{{\beta_1}' + {\beta_2}'}{2} \\ {\theta'}_s = \frac{{\alpha_2}' + {\alpha_1}'}{2}. \end{cases}$$

The blade staggered spacing can be expressed as:

$$g = s \cdot \cos\theta'.$$

3.2.3 Air Angle and Velocity Vector Geometry

The rotor absolute inlet and outlet air angles are α_1 and α_2. The rotor relative inlet and outlet air angles are β_1 and β_2. The blade velocity at the r.m.s. radius is U. C_1 and C_2 represent the rotor absolute inlet and outlet air velocities. W_1 and W_2 correspond to the inlet and outlet air velocities in the relative rotor frame. C_x is the axial velocity, and R is the degree of reaction. All these quantities are indicated in Figure 3-3. The stator inlet angle is α_2, and, as the stage is repeating, α_1 is the stator outlet angle.

The inlet incidence angle is denoted by i, and defined in Figure 3-4 as:

$$\begin{cases} \beta_1 = {\beta_1}' + i_r \\ \alpha_2 = {\alpha_2}' + i_s. \end{cases}$$

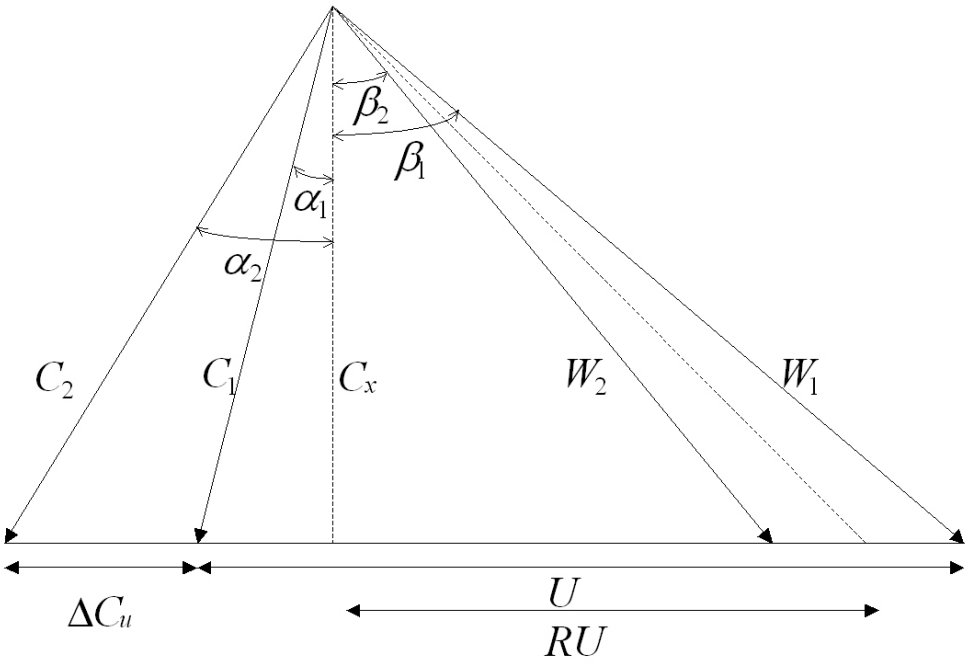

Figure 3-3: Stage velocity triangles

In a similar manner, the deviation angle links the outlet air and metal angles:

$$\begin{cases} \beta_2 = \beta_1{}' + \delta_r \\ \alpha_1 = \alpha_1{}' + \delta_s. \end{cases}$$

3.3 End-Wall Model

In [16, 11], Koch and Smith discuss the impact of hub and tip casing boundary layers on compressor stage performance. To carry out an estimate of this impact, they first compute a free-stream velocity and a free-stream efficiency that do not include end-wall effects, denoted here by the *pro* subscript.

Hub and tip boundary layers are characterized by their displacement thickness:

$$\begin{aligned} \delta_h^* &= \frac{1}{r_h C_{x_{pro}}} \int_{r_h}^{r_h+\delta_h} (C_{x_{pro}} - C_x) r dr \\ \delta_t^* &= \frac{1}{r_t C_{x_{pro}}} \int_{r_t-\delta_t}^{r_t} (C_{x_{pro}} - C_x) r dr. \end{aligned}$$

Reference [11] does not distinguish δ_h^* from δ_t^*. The displacement thickness effect of the end-wall boundary layers reduces the mass flow in the stage compared to that based on $C_{x_{pro}}$. The actual flow coefficient, $\phi = \frac{C_x}{U}$, is given by:

$$\phi = \phi_{pro} \cdot \left(1 - \frac{2\delta^*}{h}\right). \tag{3.1}$$

Boundary layers also decrease the shaft torque power dissipated to drive the flow compared to the situation with free-stream conditions over the whole geometric annulus. The decrease

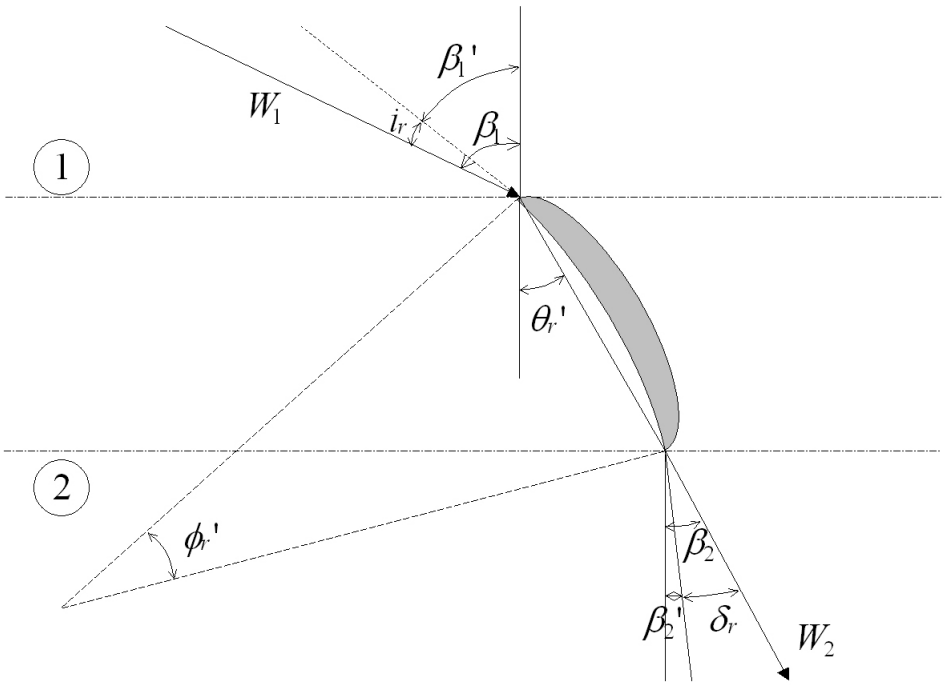

Figure 3-4: Geometry for incidence and deviation angles

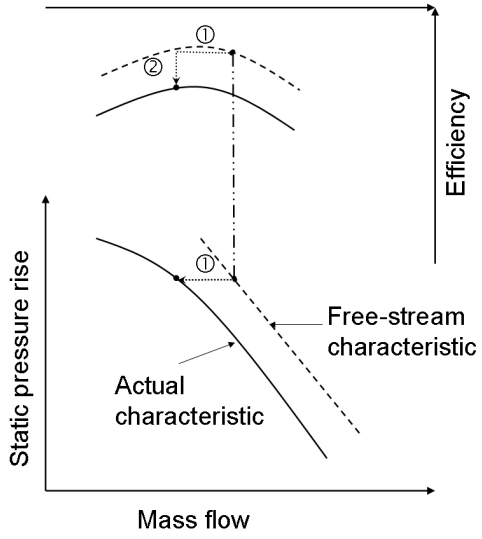

Figure 3-5: Stage characteristic constructed from free-stream performance and end-wall boundary layer [16]

in efficiency is related in [16] to the displacement thickness and to the tangential-force thickness by:

$$\eta = \eta_{pro} \frac{1 - 2\frac{\delta^*}{h}}{1 - 2\frac{\tau}{h}}. \tag{3.2}$$

Koch and Smith present in [11] correlations to compute $\frac{\delta^*}{h}$ and $\frac{\tau}{h}$ from the stage loading ratio, Ω, as shown in Figure 2-2.

The efficiency in Equation 3.2 is that corresponding to the actual characteristic curves for static pressure rise and stage efficiency, as represented in Figure 3-5. The operating point for pressure rise is determined from ϕ_{pro} using Equation 3.1, which corresponds to arrow ① on the figure.

3.4 Layout of the Algorithm

3.4.1 Algorithm Input

The algorithm used takes for input the geometric description of the stage (rotor and stator) and a non-dimensionalized form of the operating and inlet conditions. Casey [1] introduced the following typical industrial compressor stage INDUS as an example:

$$\begin{aligned}
D = 0.71, \frac{r_t}{r_h} = 1.3, R_a = 10^{-6} \\
N_r = 36, \sigma_r = 1.0, \frac{t_r}{c_r} = 0.088, \frac{\delta_{xr}}{D} = 0.0204, \frac{\epsilon_r}{D} = 0.003 \\
N_s = 36, \sigma_s = 1.0, \frac{t_s}{c_s} = 0.080, \frac{\delta_{xs}}{D} = 0.0204, \frac{\epsilon_s}{D} = 0.003 \\
{\alpha_1}' = 5.61, {\beta_1}' = 55.76, {\beta_2}' = 36.51, {\alpha_2}' = 38.33 \\
R_e = 6 \cdot 10^6, M_a = 0.45.
\end{aligned}$$

For a repeating-stage, the blade orientation is fully determined by the metal angles ${\alpha_1}'$, ${\beta_1}'$, ${\beta_2}'$ and ${\alpha_2}'$. The spool Mach number M_a and the Reynolds number R_e are defined as follows:

$$M_a = \frac{U_h}{\sqrt{\gamma R_b T}}$$

$$R_e = \frac{\rho U_h D}{\mu},$$

where ρ is the air density and μ the air dynamic viscosity.

3.4.2 Algorithm Steps

The stage loading ratio, Ω, was defined in Figure 2-2 as the ratio of the static pressure rise C_p to the stalling static pressure rise $C_{p_{max}}$:

$$\Omega = \frac{C_p}{C_{p_{max}}}. \tag{3.3}$$

Details for the computation of $C_{p_{max}}$ using [10] can be found in Section A.3.5.

To compute one point of the operating line, the algorithm goes through the following steps:

1. It chooses a value for the two-dimensional flow coefficient $\phi_{pro} = \frac{C_x}{U}_{pro}$ and guesses a value for the stage loading ratio Ω.

2. It resolves the velocity triangles for this value of ϕ_{pro}, using correlations for deviation in [14]. This yields the incidence, deviation and air angles, the velocities, and the work coefficient $\frac{C_{u2}-C_{u1}}{U}$.

3. It determines the profile losses ω with correlations in [13]. The result depends on Ω, the incidence and air angles. This allows computing the profile efficiency:

$$\eta_{pro} = 1 - \frac{\omega_r {W_1}^2 + \omega_s {C_2}^2}{2U\left(C_{u2} - C_{u1}\right)}.$$

4. It computes the end-wall boundary layer displacement thickness δ^* and tangential-force thickness τ. This yields:

   (a) the stage polytropic efficiency $\eta = \eta_{pro}\frac{1-2\frac{\delta^*}{h}}{1-2\frac{\tau}{h}}$;

   (b) the actual flow coefficient $\phi = \frac{C_x}{U}$;

   (c) the effective static pressure rise, using an effective dynamic pressure factor $\mathcal{F}_{ef}$ defined by Koch [10], $C_p = \eta\frac{C_{u2}-C_{u1}}{U}\frac{2}{{\mathcal{F}_{ef}}_r + {\mathcal{F}_{ef}}_s}$.

5. It calculates the stage loading ratio Ω with Equation 3.3 and compares it to its previous value. Steps 2 to 5 are then iterated until convergence of Ω occurs.

At the end of the iterative process, the hub flow coefficient $\nu = \frac{C_x}{U_h}$ and the stage efficiency η are determined. Following Casey [1], the pressure rise is given by:

$$\mu_y = \frac{\Delta p}{\rho {U_h}^2} = \eta\frac{C_{u2} - C_{u1}}{U}\frac{\left(\frac{r_t}{r_h}\right)^2 + 1}{2}. \tag{3.4}$$

More details about the algorithm steps are contained in Appendix A.

3.5 Program Output and Validation

Figure 3-6 exhibits the characteristics of the INDUS compressor stage mentioned in 3.4.1. Following Casey [1], the pressure rise, efficiency, losses, turning, and hub flow coefficient ν are computed from the two-dimensional flow coefficient ϕ_{pro}. The stall onset is estimated to occur at the maximum value of static pressure rise, $C_{p_{max}}$. This corresponds to the minimum value of ϕ_{pro}, and to the maximum pressure rise and turning on Figures 3-6a and 3-6e. The point of maximum efficiency on Figure 3-6b corresponds to minimum rotor and stator losses on Figures 3-6c and 3-6d, and is located a little beyond the surge point.

Figure 3-7 shows a number of curves of pressure rise with each representing the stator vanes restaggered in steps of 5 degrees to cover a range of ± 20 degrees. The figure also shows contours of efficiency. The results obtained agree with Figure 8 in [1]. Other test cases were also carried out, including comparison with data in Casey [1], to validate the algorithm at Mach numbers characteristic of industrial compressors.

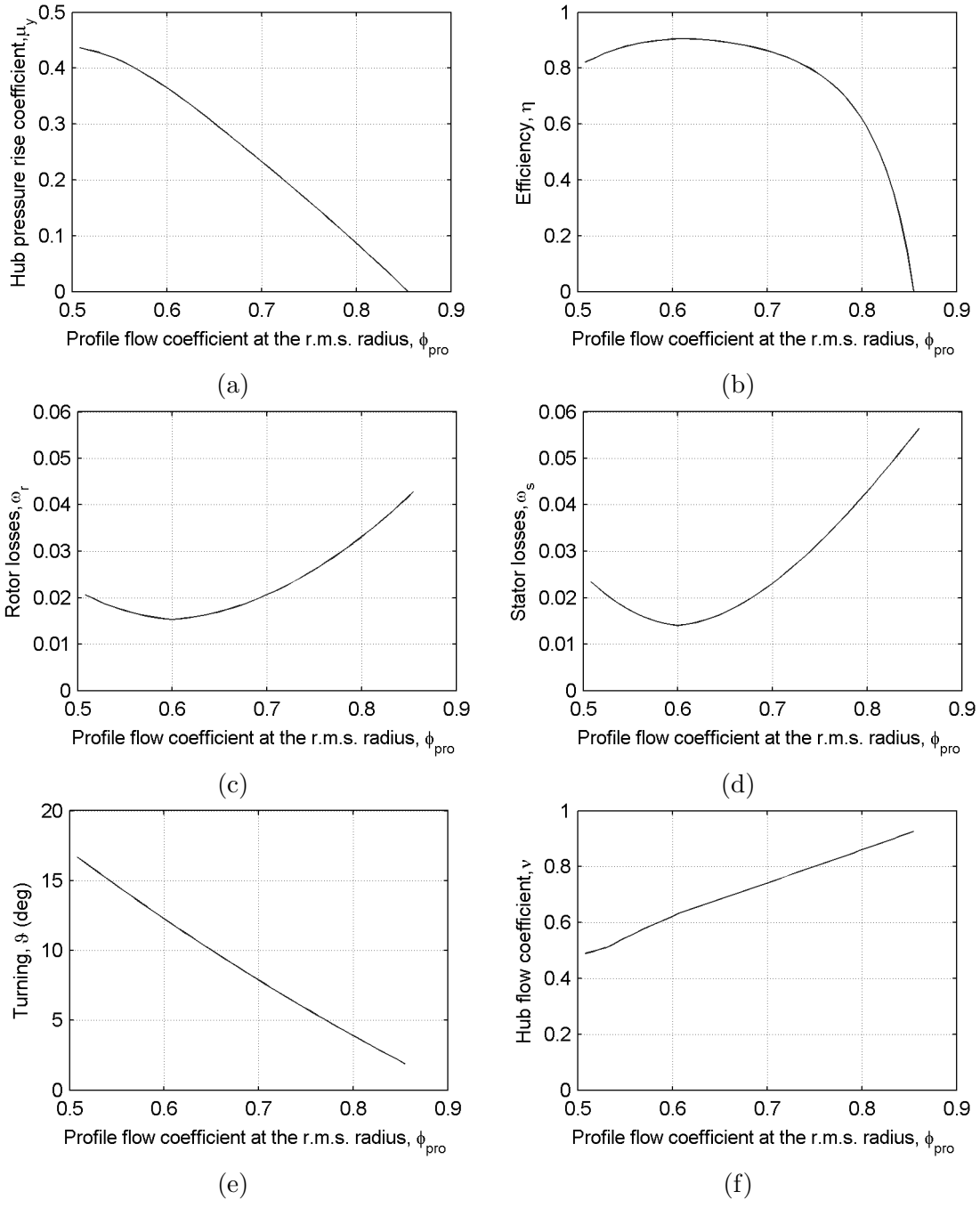

Figure 3-6: Characteristic curves for the INDUS compressor

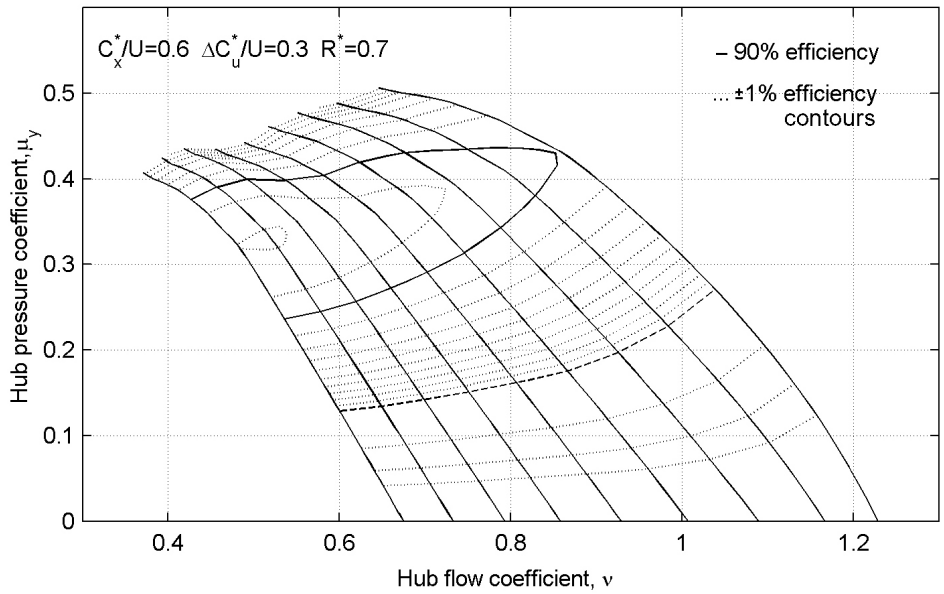

Figure 3-7: Pressure rise and efficiency when stator vanes are restaggered in steps of 5 degrees for the INDUS compressor

Chapter 4

Analysis of Sensitivity to Geometric Variability

4.1 Characterization of Geometric Variability

4.1.1 Definitions for the Probabilistic Analysis

A random variable is denoted by X. The mean value of the random variable X is represented by $\hat{\mu}_X$. The standard deviation of X is denoted by $\hat{\sigma}_X$. $\mathcal{N}(0,1)$ is the set of normal random variables with 0 as their mean value and 1 as their standard deviation, also called the set of standard normal random variables. The mean shift $\hat{S}$ of a random variable X is defined from its mean value $\hat{\mu}_X$ and its original design value X^*:

$$\hat{S}_X = \frac{\hat{\mu}_X - X^*}{X^*}.$$

The mean shift is positive when the mean value is higher than the design value, and negative when it is lower. The coefficient of variability $\hat{V}$ of a random variable X is defined as the ratio between the standard deviation $\hat{\sigma}_X$ and the mean value $\hat{\mu}_X$:

$$\hat{V}_X = \frac{\hat{\sigma}_X}{\hat{\mu}_X}.$$

For a given mean shift, the coefficient of variability (COV) scales with the standard deviation. The skewness $\hat{SK}$ of a random variable X is defined as:

$$\hat{SK}_X = \frac{\hat{\mu}[X - \hat{\mu}_X]^3}{\hat{\sigma}_X^3}.$$

Skewness is a measure of the asymmetry of the data around the sample mean. If skewness is negative, the data are spread out more to the left of the mean than to the right. If skewness is positive, the data are spread out more to the right. The skewness of the normal distribution (or any symmetric distribution) is zero.

Contrary to mean value and standard deviation, mean shift, coefficient of variability and skewness are non-dimensionalized quantities. They are used to compare figures for different compressors. Geometric variability is introduced in the INDUS compressor stage using mean values and coefficients of variability of data obtained using the IBR rotor of Garzon. The analogy is relevant even if the two compressors do not operate at same inlet conditions and

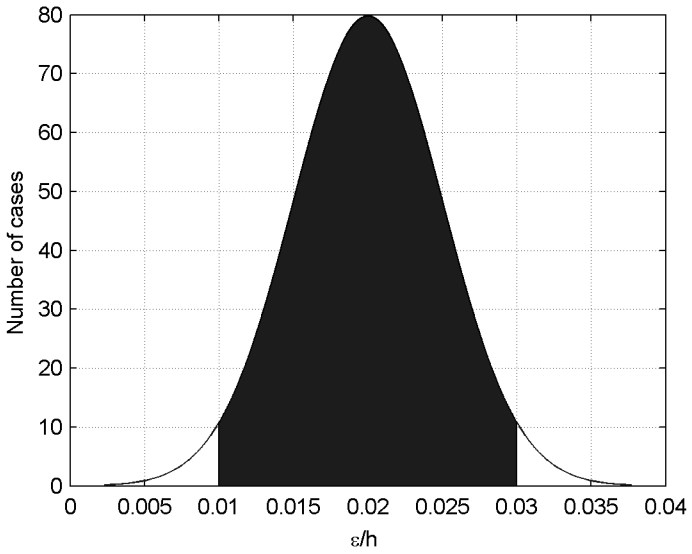

Figure 4-1: Probabilistic distribution of the ratio of tip clearance to blade height for the INDUS compressor

at same wheel speed. The sensitivity of a compressor to geometric variability corresponds to the mean shifts and the coefficients of variability of pressure rise and efficiency. Low sensitivity means low decrease in mean performance and low coefficient of variability.

4.1.2 Selection of Geometric Parameters

In this section, geometric variability is characterized and used in the mean-line model discussed in Section 3. It is assumed that geometric variability can be described as:

- variations in rotor and stator tip clearances ϵ_r and ϵ_s;
- variations in the shape of blade profiles.

Variations in tip clearances can be incorporated in the one-dimensional (mean-line) model with the proviso that the repeating-stage analysis is appropriate. However, airfoil profile variability with respect to nominal cannot be represented directly by one-dimensional geometric parameters. This variability will thus be incorporated through variations in turning angle ϑ and rotor and stator losses ω_r and ω_s, as proposed by Garzon [6]. Calculations are carried out with the compressor stage INDUS mentioned in Section 3.4.1.

4.1.3 Model for Tip Clearance Variability

For the INDUS compressor stage, the nominal ratio of tip clearance to blade height, $\left(\frac{\epsilon}{h}\right)_0$, is 2% for both rotor and stator. Tip clearance variability is taken to be represented by a gaussian distribution of mean value $\left(\frac{\epsilon}{h}\right)_0$ and coefficient of variability 50%. The random tip clearances can be written as:

$$\frac{\epsilon_r}{h}(X_1) = \left(\frac{\epsilon_r}{h}\right)_0 \cdot (1 + 50\% X_1) \tag{4.1}$$

$$\frac{\epsilon_s}{h}(X_2) = \left(\frac{\epsilon_s}{h}\right)_0 \cdot (1 + 50\% X_2)\,, \tag{4.2}$$

where

- $\left(\frac{\epsilon_r}{h}\right)_0 = \left(\frac{\epsilon_s}{h}\right)_0 = 2\%$;
- $X_1, X_2 \in \mathcal{N}(0,1)$;

The shaded area in Figure 4-1 represents the probability (95%) that the random tip clearance ratio is located between 1% and 3%. Although there is a probability for the tip clearance ratio to be negative, the value is low enough ($3.2 \cdot 10^{-3}\%$), so that its effect was neglected in the calculation.

4.1.4 Blade Profile Variability

Garzon [6] estimated the blade profile variability by exploiting the results of computations based on a set of blade measurements. An integrally-bladed rotor (IBR) consisting of 56 blades with an inlet tip radius of 9.87 inches and a tip-to-hub ratio of 1.17 was considered. Surface measurements of blades from four separate rotors had been carried out using a scanning coordinate-measuring machine (CMM). Each blade was measured at 13 different radial locations, with CMM measurements of 112 points at each station. A principal component analysis (PCA) allows expressing the actual coordinate X of any point that is part of the two-dimensional profile edge as:

$$X = \boldsymbol{x}^0 + \overline{\boldsymbol{x}} + \sum_{i=1}^{K} \sqrt{\lambda_i} Z_i \boldsymbol{v}_i,$$

where

- $\boldsymbol{x}^0$ is the nominal geometry;
- $\overline{\boldsymbol{x}}$ is the shift to the nominal geometry;
- $\forall i \in [1, K], Z_i \in \mathcal{N}(0,1)$;
- λ_i and $\boldsymbol{v}_i$ are respectively the i^{th} eigenvalue and the corresponding eigenvector of the scatter matrix of measurements.

The coefficients λ_i are determined by the PCA analysis: each of them corresponds to one of $K = 2 * 112$ modes that influence the profile geometry. The factor 2 comes from the two-dimensional aspect of the analysis.

Garzon calculated the impact of blade profile variability on turning and losses using these data and the quasi-2D cascade analysis code MISES. As described in his thesis, he increased the geometric variations by a factor of five, since it was found that this was more representative of variability in industrial blades than in those forming the sample pool. The sample blades were manufactured with a different method not used for actual blades. More details can be found in Appendix B of [6], and in a study of Garzon and Darmofal [7]. Garzon assumed that the deviation modes are independent: the Z_i are independent standard normal random variables.

A Monte Carlo simulation using MISES was run for the IBR rotor for several incidence angles. Here the term "incidence angle" i_n refers to the difference between actual flow angle β_1 and nominal inlet flow angle ${\beta_1}^*$:

$$i_n = \beta_1 - {\beta_1}^*.$$

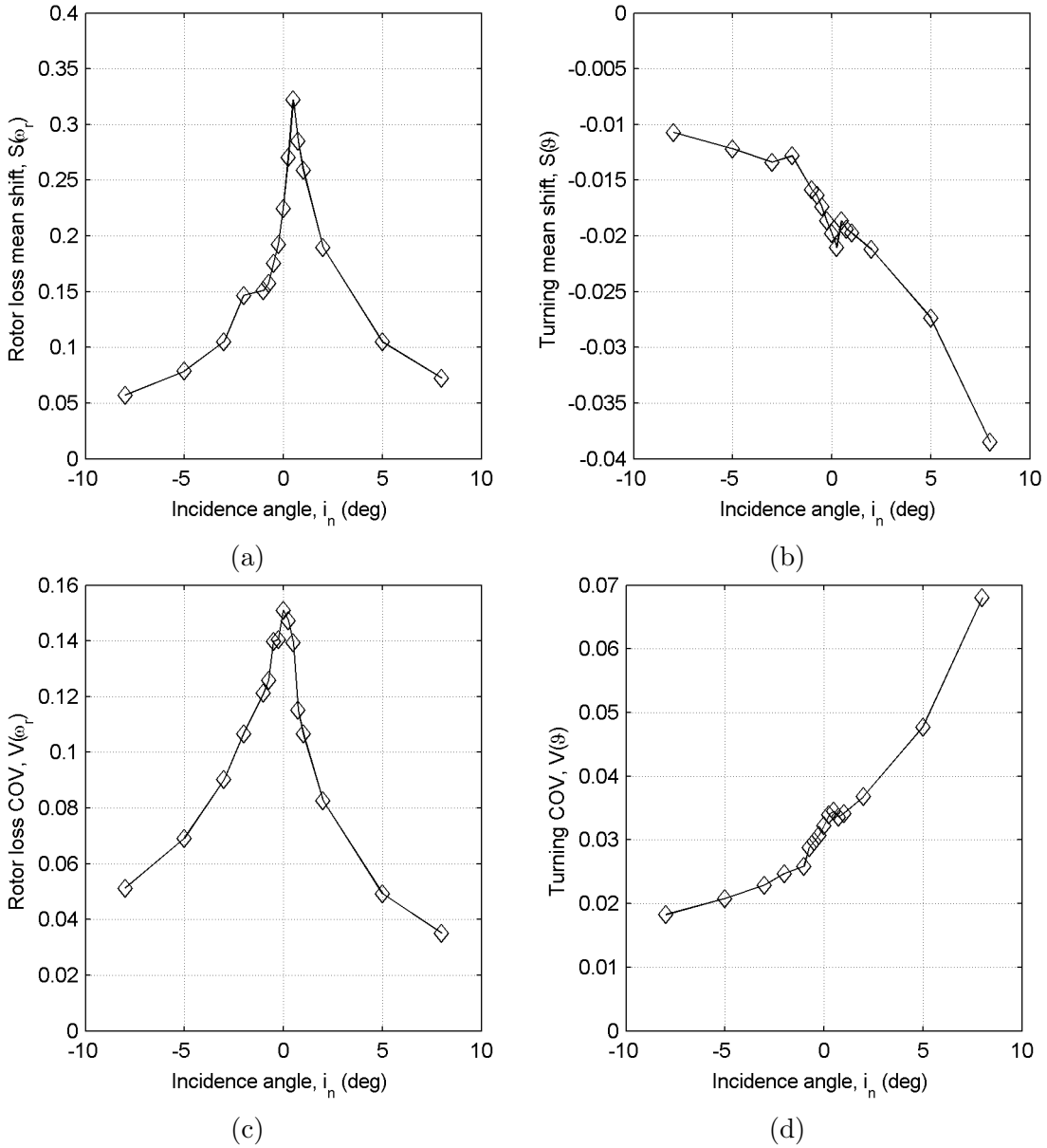

Figure 4-2: Normalized rotor losses and turning angle vs. incidence. Mean shift and coefficient of variability obtained by Garzon for the IBR rotor [6]

For each incidence angle, Garzon ran a set of Monte Carlo simulations, and recorded the turning and the rotor losses. The results were presented in Figure 2-4 and we make use of those results in the mean-line analysis here. For each incidence angle, the coefficient of variability $\hat{V}$ and the mean shift $\hat{S}$ are computed for losses and turning. The values obtained appear in Figure 4-2. In the range of incidence considered, Figures 4-2a and 4-2b indicate that the blade profile variability increases mean rotor losses and decreases mean turning. Both trends imply a decrease in stage pressure rise and efficiency. At the design incidence $i_n = 0$, the coefficients of variability are 15% for rotor losses and 3.2% for turning.

Figure 4-2a indicates a peak in loss mean shift at design incidence. The peak in loss coefficient of variability at design incidence reported in Figure 4-2c is associated with the minimum of the mean value of rotor losses (see Figure 2-4a) and the relatively constant value of the standard deviation at design incidence (see Figure 2-4c).

4.1.5 Model for Blade Profile Variability

The model used for the variations in turning and rotor and stator losses was as follows:

- Blade profile variabilities were incorporated by changing the values of turning and losses in accord with the mean shifts and coefficients of variability found by Garzon.
- For each incidence angle, the mean value of the turning or losses is the original mean value multiplied by the mean shift reported in Figure 4-2.
- For each incidence angle, the turning and losses are normal random variables, and their coefficient of variability is equal to those appearing in Figure 4-2.
- In the absence of other information, the mean shifts and the coefficients of variability for the stator are assumed to be the same as for the rotor.
- If a correction on a first parameter has an impact on a second parameter that is also corrected, the second parameter is corrected on the basis of its new value. Thus, tip clearances, turning and losses are not completely independent values in the algorithm.

Three independent standard normal random variables are introduced: X_3 for rotor turning, X_4 for rotor losses, and X_5 for stator losses. Because we consider a repeating-stage, with identical inlet and outlet angles, stator turning variability is already included in rotor turning variability. After some algebra, the previous assumptions can be summarized in the following equations:

$$\vartheta(i_n) = \vartheta_0(i_n) \cdot \left(\hat{S}_\vartheta(i_n) + 1\right) \cdot \left(1 + \hat{V}_\vartheta(i_n) \cdot X_3\right) \tag{4.3}$$

$$\omega_r(i_n) = \omega_{r0}(i_n) \cdot \left(\hat{S}_{\omega_r}(i_n) + 1\right) \cdot \left(1 + \hat{V}_{\omega_r}(i_n) \cdot X_4\right) \tag{4.4}$$

$$\omega_s(i_n) = \omega_{s0}(i_n) \cdot \left(\hat{S}_{\omega_s}(i_n) + 1\right) \cdot \left(1 + \hat{V}_{\omega_s}(i_n) \cdot X_5\right), \tag{4.5}$$

where

$$X_3, X_4, X_5 \in \mathcal{N}(0,1).$$

Influence	ϵ_r	ϵ_s	ϑ	ω_r	ω_s
Rotor tip clearance ϵ_r	x	-	-	-	-
Stator tip clearance ϵ_s	-	x	-	-	-
Turning ϑ	+	+	x	-	-
Rotor losses ω_r	+	+	-	x	-
Stator losses ω_s	+	+	+++	-	x

x crossed term, - no influence, + little influence, +++ significant influence

Table 4.1: Interdependence of variables

4.2 Implementation of Variability in the Algorithm

4.2.1 Equations

The inclusion of geometric variability in the algorithm requires five independent standard normal random variables X_1, X_2, X_3, X_4 and X_5. Equations 4.1, 4.2, 4.3, 4.4 and 4.5 are completed by adding a factor for mean shift $\Gamma^{\hat{S}}$, and a factor for coefficient of variability $\Gamma^{\hat{V}}$. Five factors for coefficient of variability are introduced, for rotor and stator losses and tip clearances, and turning. As the mean value of tip clearances is not modified, only three factors for mean shift are introduced, for rotor and stator losses and turning. Included in the $[0, 1]$ range, these factors indicate which fraction of the IBR correlation mean shift and variability is retained. Three cases are of special interest:

- When $\Gamma^{\hat{S}} = 1$ and $\Gamma^{\hat{V}} = 1$, the correlations given by Garzon are used.
- When $\Gamma^{\hat{S}} = 1$ and $\Gamma^{\hat{V}} = 0$, only the mean shift is considered, so the analysis is no longer probabilistic.
- When $\Gamma^{\hat{S}} = 0$ and $\Gamma^{\hat{V}} = 1$, only the variability around the nominal value is considered.

The final set of equations is:

$$\begin{cases} \frac{\epsilon_r}{h} &= \left(\frac{\epsilon_r}{h}\right)_0 \cdot \left(1 + \Gamma^{\hat{V}}_{\epsilon_r} \cdot 50\% \cdot X_1\right) \\ \frac{\epsilon_s}{h} &= \left(\frac{\epsilon_s}{h}\right)_0 \cdot \left(1 + \Gamma^{\hat{V}}_{\epsilon_s} \cdot 50\% \cdot X_2\right) \\ \vartheta(i_n) &= \vartheta_0(i_n) \cdot \left(\Gamma^{\hat{S}}_{\vartheta} \cdot \hat{S}_{\vartheta}(i_n) + 1\right) \cdot \left(1 + \Gamma^{\hat{V}}_{\vartheta} \cdot \hat{V}_{\vartheta}(i_n) \cdot X_3\right) \\ \omega_r(i_n) &= \omega_{r0}(i_n) \cdot \left(\Gamma^{\hat{S}}_{\omega_r} \cdot \hat{S}_{\omega_r}(i_n) + 1\right) \cdot \left(1 + \Gamma^{\hat{V}}_{\omega_r} \cdot \hat{V}_{\omega_r}(i_n) \cdot X_4\right) \\ \omega_s(i_n) &= \omega_{s0}(i_n) \cdot \left(\Gamma^{\hat{S}}_{\omega_s} \cdot \hat{S}_{\omega_s}(i_n) + 1\right) \cdot \left(1 + \Gamma^{\hat{V}}_{\omega_s} \cdot \hat{V}_{\omega_s}(i_n) \cdot X_5\right), \end{cases}$$

where

$$X_1, X_2, X_3, X_4, X_5 \in \mathcal{N}(0, 1).$$

These corrections are expressed in terms of incidence angle i_n whereas the mean-line model works with the two-dimensional flow coefficient ϕ_{pro}. Therefore, a link between both quantities has to be established. This is detailed in the Appendix, Section B.2.2.

4.2.2 Interdependence of Variables

When the value of a variable is changed to account for geometric variability, this also induces minor modifications of other variables. Table 4.1 summarizes these dependences. Whereas

Geometric parameter		*Mean shift in pressure* $100 \cdot \hat{S}(\mu_y)$	*Mean shift in efficiency* $100 \cdot \hat{S}(\eta)$		*Mean shift in pressure* $100 \cdot \hat{S}(\mu_y)$	*Mean shift in efficiency* $100 \cdot \hat{S}(\eta)$
Rotor tip clearance ϵ_r	$+2\sigma$	-0.81	-0.81	-2σ	0.79	0.79
Stator tip clearance ϵ_s	$+2\sigma$	-0.31	-0.31	-2σ	0.31	0.31
Tip clearances ϵ_r, ϵ_s	$+2\sigma$	-1.12	-1.12	-2σ	1.09	1.09
Rotor losses ω_r	$+2\sigma$	-1.58	-1.58	-2σ	0.38	0.39
Stator losses ω_s	$+2\sigma$	-0.76	-0.76	-2σ	0.19	0.19
Losses ω_r, ω_s	$+2\sigma$	-2.35	-2.35	-2σ	0.58	0.58
Turning ϑ	-2σ	-6.63	0.03	$+2\sigma$	3.29	-0.10

Table 4.2: Deterministic sensitivity analysis for the INDUS compressor at design incidence by assigning geometric parameters to their $\pm 2\sigma$ values

the impact of tip clearances on turning and losses is often negligible, the influence of turning variations on stator losses is clear. The origin of these relationships is detailed in Section B.2.3.

4.2.3 Probabilistic Input

A Monte Carlo simulation using 2500 trials has been carried out for the INDUS compressor. Figure 4-3 compares the variability of the inputs between the Monte Carlo simulation of the INDUS compressor and the IBR case of Garzon [6]. If tip clearances, losses and turning were independent variables as in the work of Garzon, the "MCS" and "Garzon" curves would be superimposed in Figures 4-3c, d, e, f, i and k. The agreement is good, but not perfect. Indeed, when the value of a variable is changed using correlations from Garzon through the equations of Section 4.2.1, it may have already altered by the application of correlations to another variable. The more a variable is influenced by others as reported in Table 4.1, the wider is the discrepancy between the "MCS" and the "Garzon" curves in Figure 4-3. For instance, the dependence of stator losses on turning appears in the discrepancy for mean shift and coefficient of variability in Figures 4-3d and 4-3f.

Figure 4-3 also shows a "Shift" curve that corresponds to a deterministic simulation of the INDUS compressor accounting for mean shift, but not for variability. Figures 4-3c, d and i reveal no visible difference in mean shift of input parameters between the Monte Carlo simulation and the "Shift" case. The "MCS" and "Shift" curves are also superimposed in Figures 4-3a, b and g.

4.3 Performance Results

4.3.1 Sensitivity to Individual Parameters

To explore which input parameters affect performance the most, 2σ values of tip clearances, losses and turning are considered. This is equivalent to assigning successively the values 2 and -2 to random variables X_1, X_2, X_3, X_4 and X_5 in the equations of Section 4.2.1. Geometric parameters are varied one at a time. Rotor and stator effects are also put together for tip clearances and losses. Table 4.2 summarizes the results at design incidence angle $i_n = 0$.

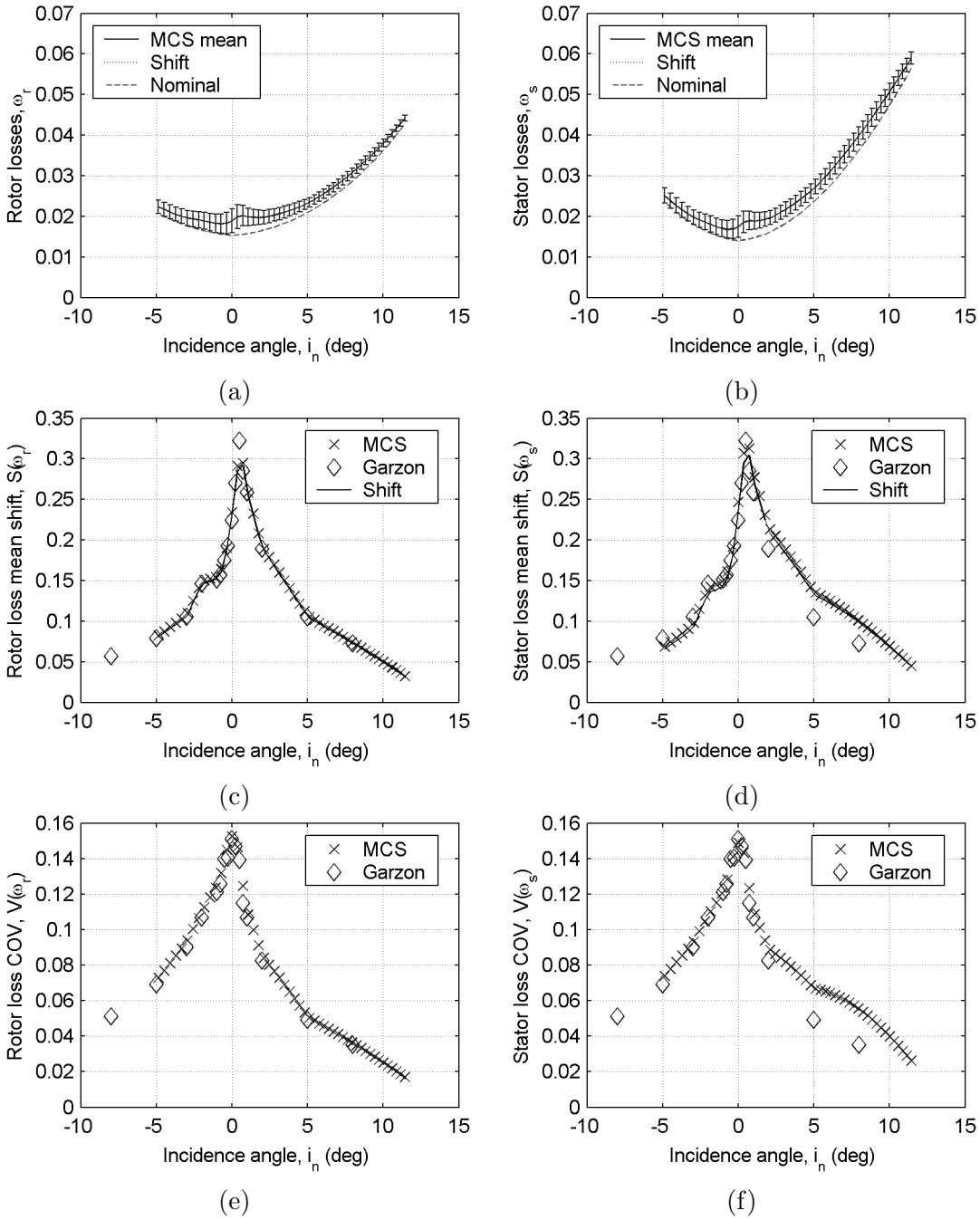

Figure 4-3: Probabilistic distribution of the input parameters for the Monte Carlo simulation. "MCS" is the Monte Carlo simulation for the INDUS compressor. "Garzon" is the Monte Carlo simulation for the IBR rotor as reported by Garzon [6]. "Shift" is the deterministic simulation of the INDUS compressor where only mean shift is accounted for.

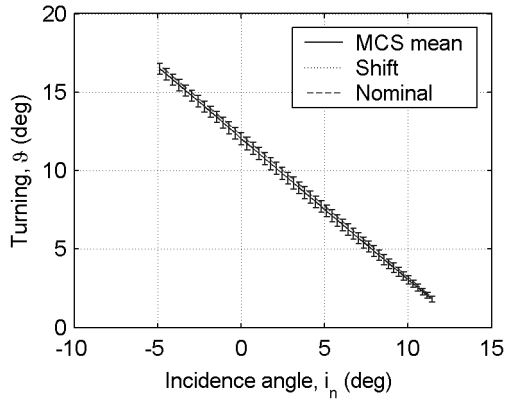

(g)

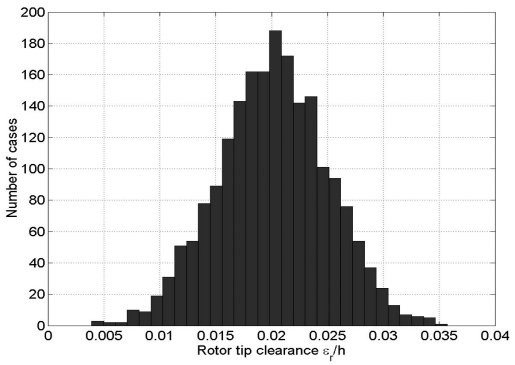

(h) Probabilistic distribution of rotor tip clearance

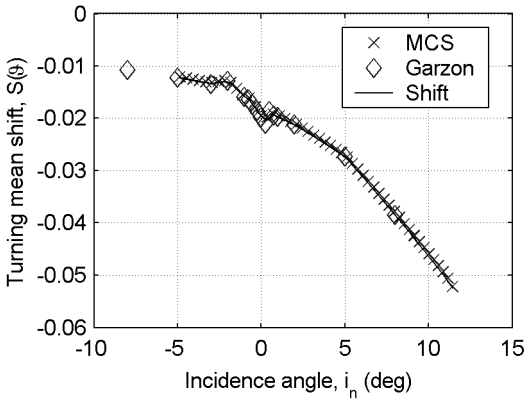

(i)

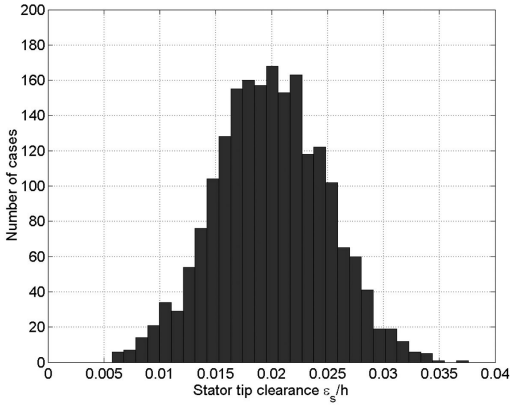

(j) Probabilistic distribution of stator tip clearance

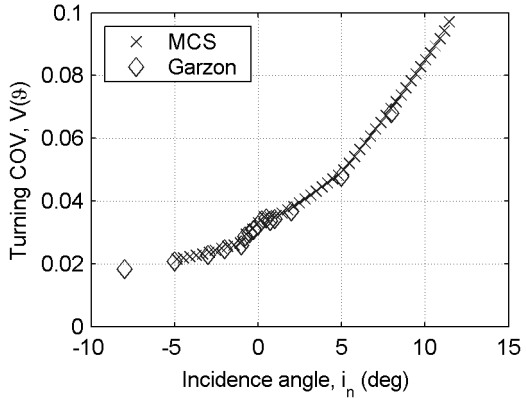

(k)

Figure 4-3 (continued): Probabilistic distribution of the input parameters for the Monte Carlo simulation. "MCS" is the Monte Carlo simulation for the INDUS compressor. "Garzon" is the Monte Carlo simulation for the IBR rotor as reported by Garzon [6]. "Shift" is the deterministic simulation of the INDUS compressor where only mean shift is accounted for.

The impact of turning on efficiency is negligible compared to tip clearance and losses, whereas it is the key driver for pressure rise. Rotor tip clearance and losses are more important than stator tip clearance and losses. The effects of tip clearances and losses are of roughly the same magnitude. Table 4.2 shows that the mean shifts due to variations in tip clearances and losses of stage efficiency and pressure rise are similar for pressure rise and efficiency. Equation 3.4 can be rewritten to indicate the dependence of variables:

$$\mu_y \simeq \lambda \cdot \eta\left(\epsilon_r, \epsilon_s, \omega_r, \omega_s\right) \cdot \left(\frac{C_{u2} - C_{u1}}{U}\right)(\vartheta)\,. \tag{4.6}$$

The linearity of Equation 4.6 implies that the mean shifts due to tip clearances or losses are approximately equal for pressure rise and efficiency. However, Equation 4.6 is only an approximation, because the dependence of efficiency on turning appears in Table 4.2.

4.3.2 Baseline Monte Carlo Simulation

Figure 4-4 shows the mean value, the mean shift, the coefficient of variability and the skewness for the pressure rise and efficiency of the INDUS compressor stage. The Monte Carlo simulation for the INDUS compressor is represented on Figure 4-4 as the "MCS" curve. Figure 4-4 also shows a "Shift" curve that corresponds to a deterministic simulation of the INDUS compressor accounting for mean shift, but not for variability.

At design incidence, Figures 4-4c and 4-4d show that geometric variability causes a 1% decrease in efficiency, and a 2.5% decrease in pressure rise. On theses figures, the "Shift" curve is almost superimposed with the "MCS" curve. This indicates that the introduction of the mean shift accounts for most of the mean performance degradation, whereas the impact of the probabilistic component (the input coefficient of variability) remains limited.

4.3.3 Relative Importance of Sources of Variability

Figure 4-5 exhibits the values of the mean shift of pressure rise and efficiency for different sources of variability. Figures 4-5c and 4-5d show that the average effect of tip clearances on pressure rise and efficiency is negligible. Figure 4-5b shows that losses account for most of the 1.25% drop in efficiency at design incidence $i_n = 0$. Adding the 1.5% decrease in pressure rise due to turning observed in Figure 4-5a, the 2.5% drop in pressure rise reported in the same figure can be justified. Finally, Figures 4-5e and 4-5f show that rotor losses account for two third and stator losses for one third of the drop in pressure rise.

Figure 4-6 exhibits the values of the coefficient of variability (COV) of pressure rise and efficiency for different sources of variability. Figure 4-6b shows that turning effects can be neglected compared to tip clearance effects and losses for efficiency COV in the $[-5, 2]$ incidence range. However, Figure 4-6a indicates that turning dominates over tip clearance effects and losses for pressure rise COV within the examined incidence range. At design incidence, the impacts of losses and tip clearances are of the same magnitude according to Figures 4-6c and 4-6d. Figures 4-6e, f, g and h show that rotor losses dominate over stator losses, and that rotor tip clearance effects dominate over stator tip clearance effects. Table 4.3 summarizes the results of Figures 4-5 and 4-6 at design incidence. The variability of 2.5% in pressure rise is dominated by turning, while losses and tip clearances are the main factors for efficiency and account for a variability of 0.7%.

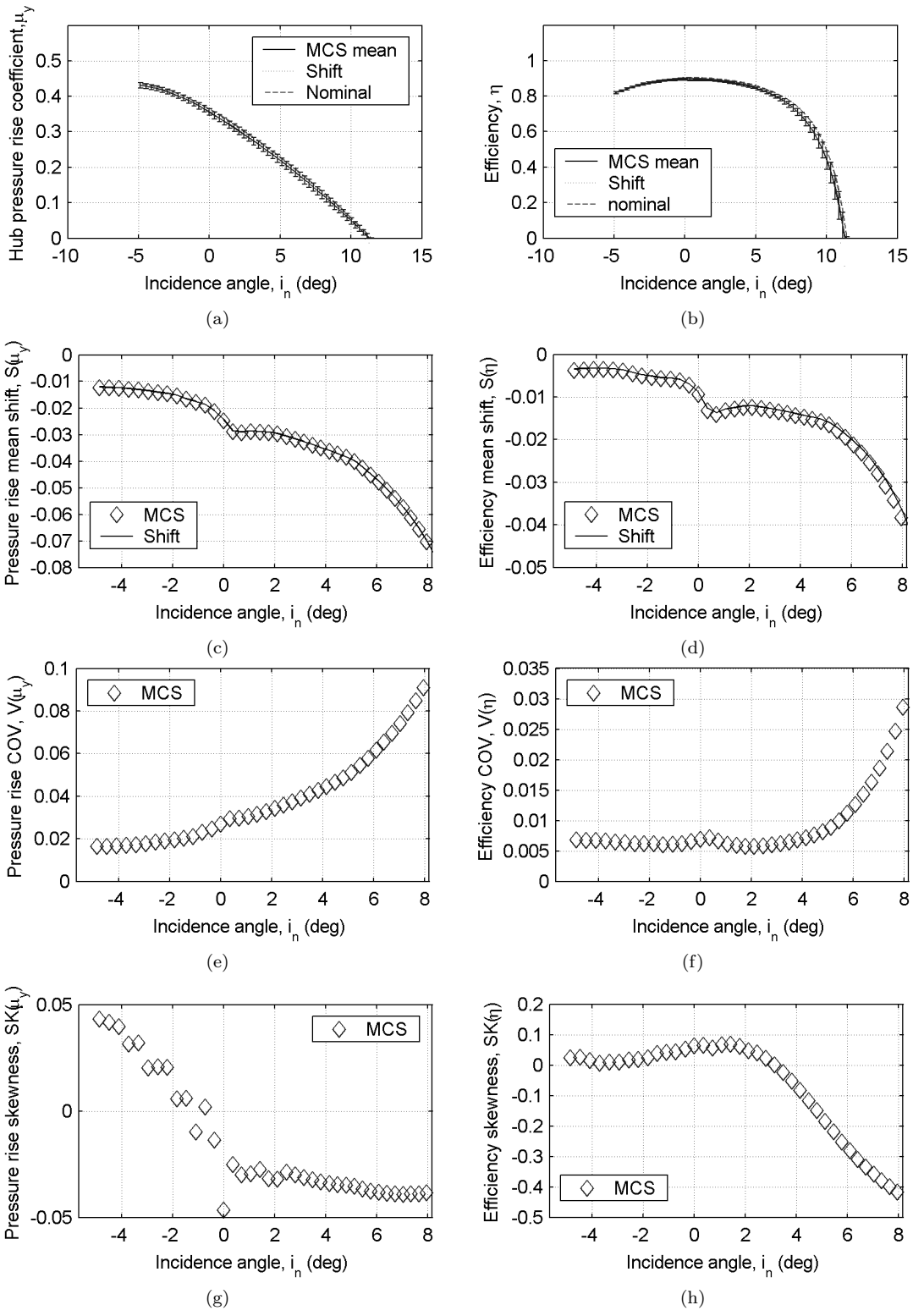

Figure 4-4: Probabilistic results for pressure rise and efficiency. "MCS" is the Monte Carlo simulation for the INDUS compressor. "Shift" is the deterministic simulation of the INDUS compressor where only mean shift is accounted for.

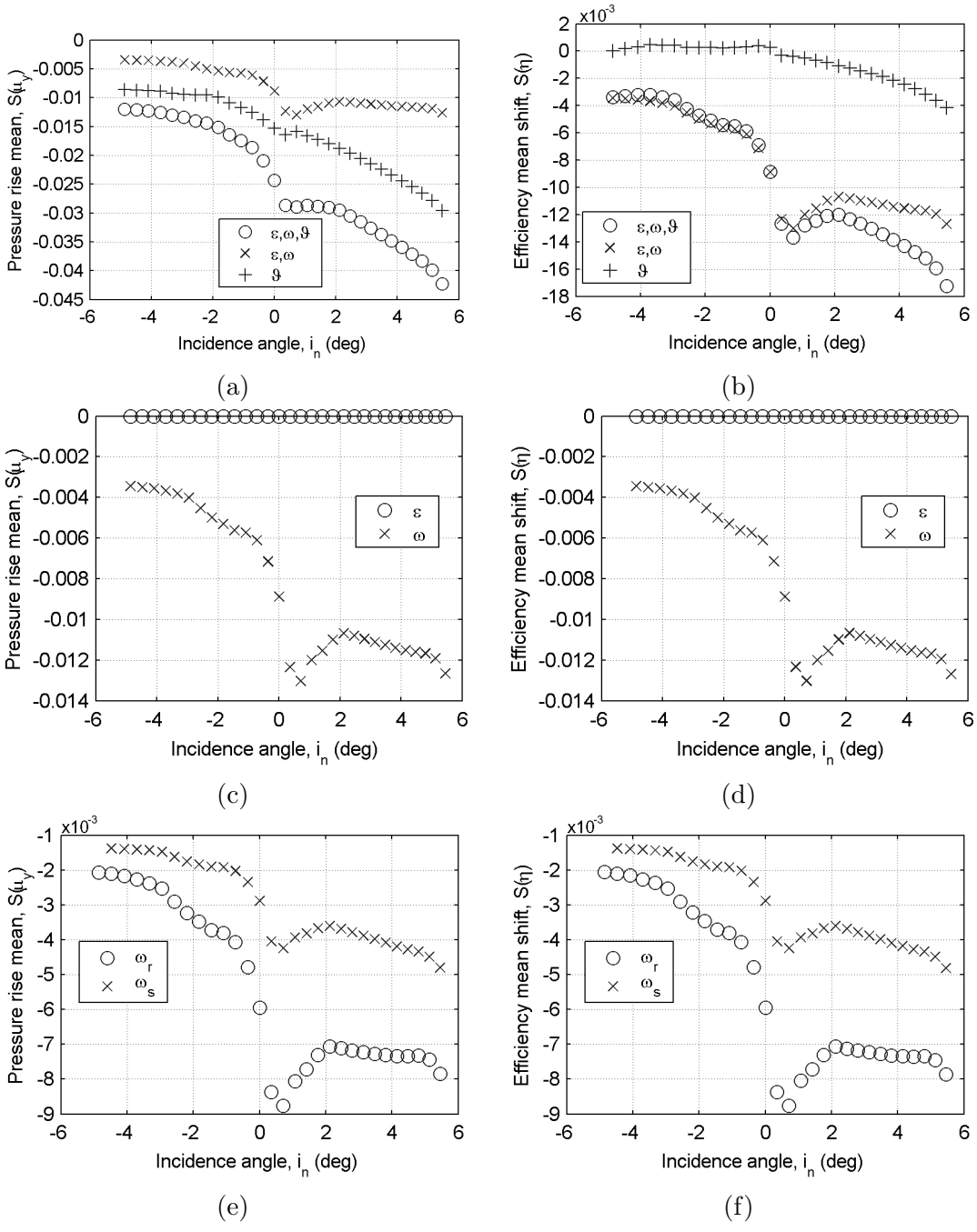

Figure 4-5: Mean shift for different sources of variability for the INDUS compressor. ϵ is the variability of tip clearance, ω is the variability of the losses, ϑ is the variability of the turning.

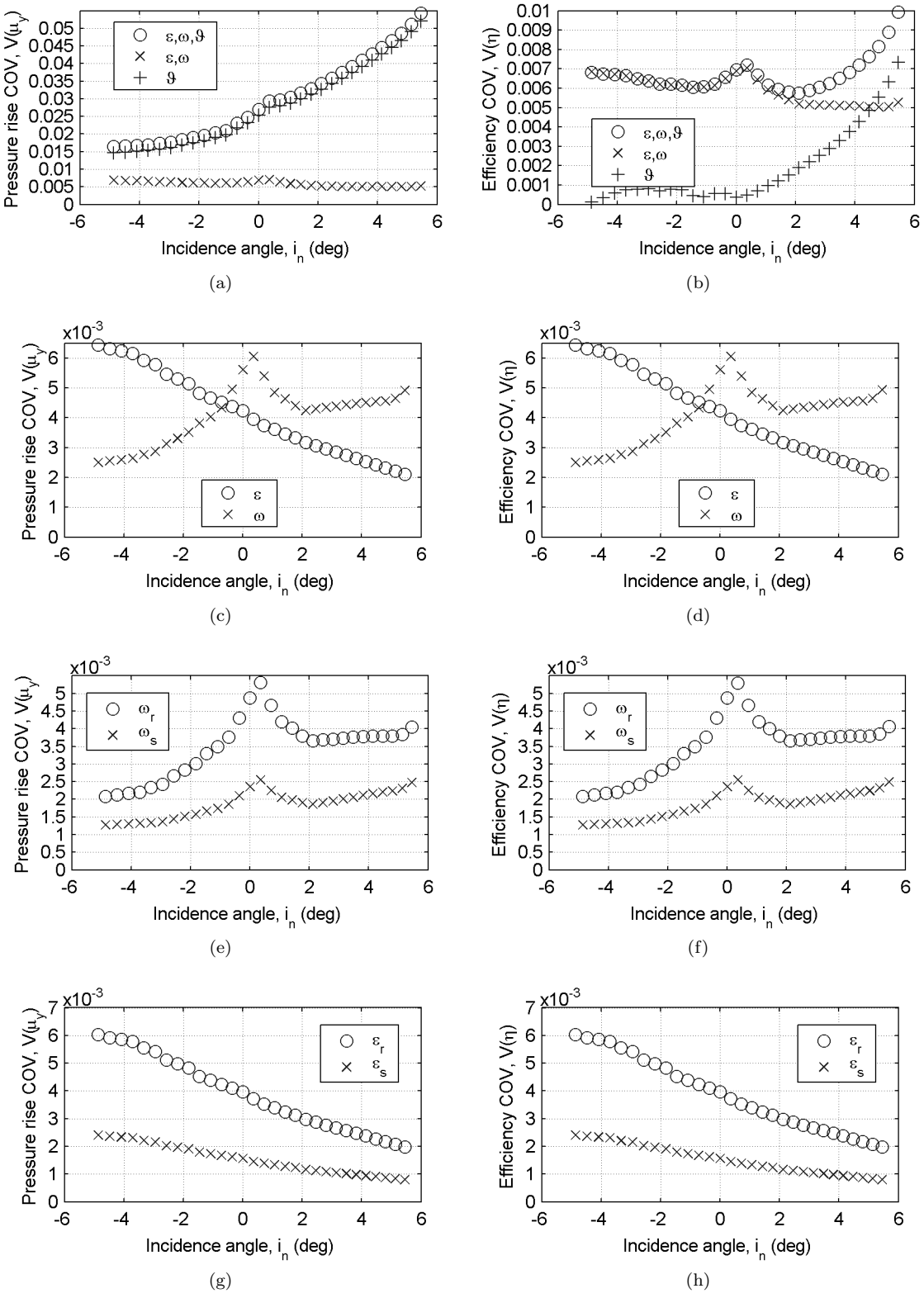

Figure 4-6: Coefficient of variability (COV) for different sources of variability for the INDUS compressor. ϵ is the variability of tip clearance, ω is the variability of the losses, ϑ is the variability of the turning.

Geometric parameter	*Mean shift for pressure* $100 \cdot \hat{S}(\mu_y)$	*COV for pressure* $100 \cdot \hat{V}(\mu_y)$	*Mean shift for efficiency* $100 \cdot \hat{S}(\eta)$	*COV for efficiency* $100 \cdot \hat{V}(\eta)$
All applied	-2.48	2.63	-0.94	0.69
Rotor tip clearance ϵ_r	0.01	0.40	0.01	0.40
Stator tip clearance ϵ_s	0.00	0.16	0.00	0.16
Tip clearances ϵ_r, ϵ_s	0.00	0.42	0.00	0.42
Rotor losses ω_r	-0.59	0.48	-0.59	0.48
Stator losses ω_s	-0.29	0.24	-0.29	0.24
Losses ω_r, ω_s	-0.88	0.56	-0.88	0.56
Turning ϑ	-1.60	2.49	0.01	0.04

Table 4.3: Mean shift and coefficient of variability of the Monte Carlo analysis at design incidence for the INDUS compressor

4.3.4 Variation of Mean Shift Factor

Section 4.3.2 indicated that the degradation in mean performance is mostly due to the mean shift of input parameters, as variability effects are negligible. In this section, the performances for three levels of input mean shift are compared:

1. Variability and mean shift included ($\Gamma^{\hat{V}} = 1, \Gamma^{\hat{S}} = 1$): this is the baseline Monte Carlo simulation mentioned at Section 4.3.2.
2. Variability and half the mean shift taken into account ($\Gamma^{\hat{V}} = 1, \Gamma^{\hat{S}} = 0.5$).
3. Variability only taken into account ($\Gamma^{\hat{V}} = 1, \Gamma^{\hat{S}} = 0$).

Figures 4-7a and 4-7b show that in the absence of input mean shift ($\Gamma^{\hat{S}} = 0$), the mean performances in pressure rise and efficiency are not significantly affected by input variability. This means for instance that the degradation of performance due to a higher tip clearance is compensated by the improvement due to a lower tip clearance. Equation 3.2 can be written as:

$$\begin{aligned} \frac{\eta}{\eta_{pro}} &= \frac{1 - 2\frac{\delta^*}{h}}{1 - 2\frac{\tau}{h}} \\ &\sim 1 - 2\frac{\delta^*}{h} + 2\frac{\tau}{h} \\ &\sim 1 - \frac{\delta^*}{h}, \end{aligned}$$

because $\tau \sim \frac{\delta^*}{2}$. Equations in Section A.3.4 indicate that boundary layer thickness δ^* is a linear function of tip clearance ϵ within the simple model used. The stage efficiency can thus be approximated as a linear function of tip clearances. Besides, the input distribution of tip clearances is symmetric. This explains why the mean efficiency is the same as the design efficiency when $\Gamma^{\hat{S}} = 0$. The quasi-linear relationship between pressure rise and efficiency with respect to tip clearance expressed in Equation 4.6 extends this result to the pressure rise.

Figures 4-7a and 4-7b also reveal that the performance degradation due to the introduction of mean shift is linear with the factor for mean shift $\Gamma^{\hat{S}}$. Figure 4-7c indicates a

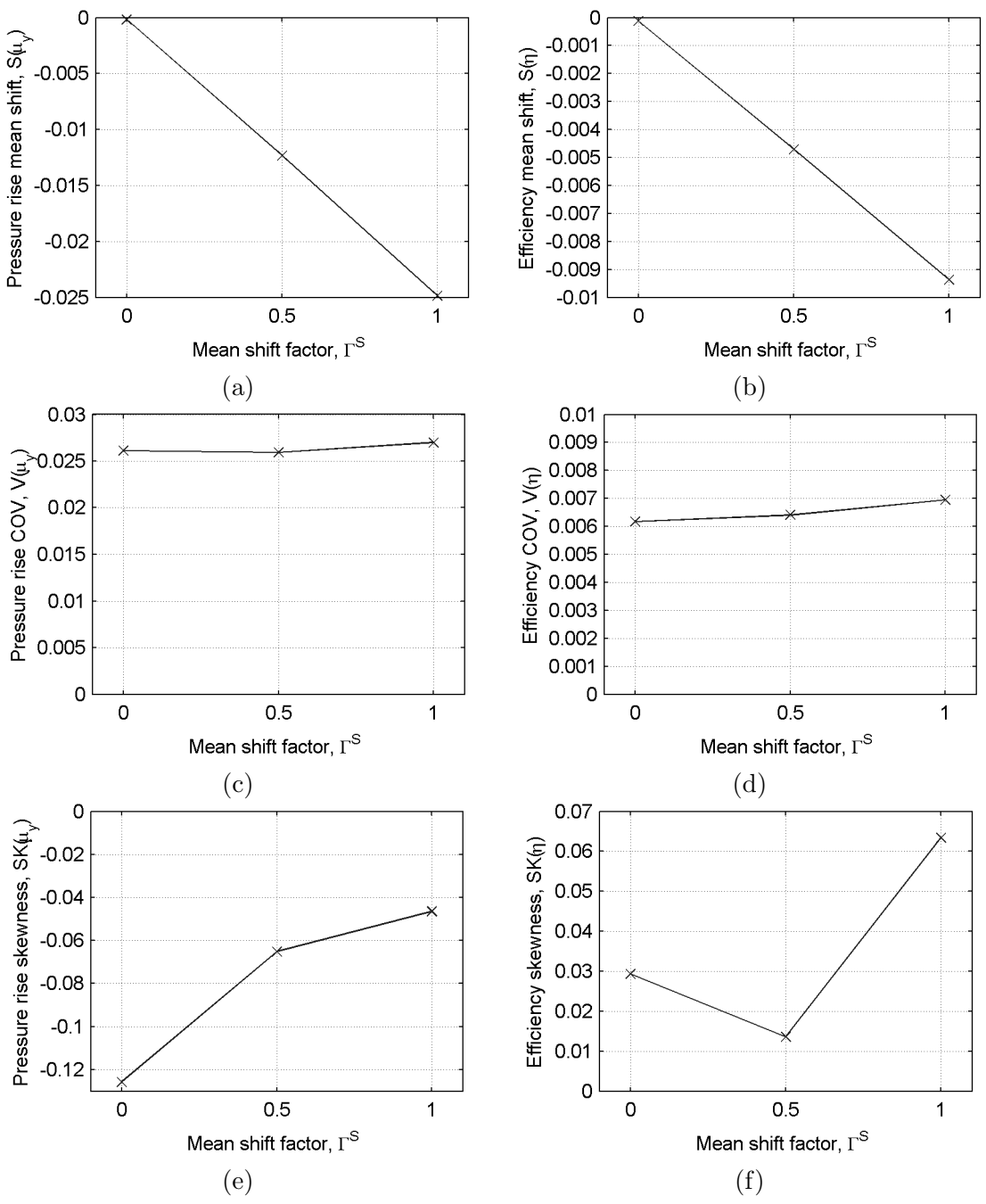

Figure 4-7: Performance dependence on the mean shift factor for the INDUS compressor at design incidence. Pressure rise and efficiency are calculated using Monte Carlo simulation, and compared through their mean shift, coefficient of variability (COV) and skewness.

4% increase of the pressure rise coefficient of variability, and Figure 4-7d a 14% increase of the efficiency coefficient of variability. These increases cannot be explained only by the decrease in mean pressure rise and efficiency. Thus the standard deviations of pressure rise and efficiency increase when the mean shift factor increases. Why the pressure rise coefficient of variability is reduced when $\Gamma^{\hat{S}}$ increases from $\Gamma^{\hat{S}} = 0$ to $\Gamma^{\hat{S}} = 0.5$ has yet to be explained.

4.3.5 Sensitivity of Different Compressor Designs to Geometric Variability

Figure 4-8 shows the variations in pressure rise and efficiency at design incidence for a series of compressors derived from INDUS. Following Casey [1], parameters varied were the design degree of reaction R^* and the design work coefficient $\left(\frac{C_{u2}-C_{u1}}{U}\right)^*$. Three values of design degree of reaction R^* were examined: 0.5, 0.7 and 0.9. Three values of design work coefficient $\left(\frac{C_{u2}-C_{u1}}{U}\right)^*$ were also examined: 0.2, 0.4 and 0.6, leading to 9 combinations. INDUS is characterized by $R^* = 0.5$ and by $\left(\frac{C_{u2}-C_{u1}}{U}\right)^* = 0.4$. The design value of the two-dimensional flow coefficient is set to ${\phi_{pro}}^* = 0.6$. As explained in Section A.2.3, the variation in R^* and $\left(\frac{C_{u2}-C_{u1}}{U}\right)^*$ is equivalent to a modification of blade metal angles. Each data symbol on Figure 4-8 corresponds to a Monte Carlo simulation of 2000 trials.

Figures 4-8a and 4-8b show the mean pressure rise and the mean efficiency at design incidence for different work coefficients and degrees of reaction. Figures 4-8c and 4-8d show that the decrease in pressure rise and efficiency due to variability is lower for stages with higher work coefficient and lower degree of reaction. Figures 4-8e and 4-8f indicate that the coefficient of variability is lower for a higher work coefficient and a lower degree of reaction.

4.3.6 Variation of Blade Aspect Ratio

A brief study was also carried out to examine the effects of aspect ratio. Figure 4-9 shows the variations in pressure rise and efficiency at design incidence for a series of compressors derived from INDUS. The compressors differ in chord, and thus in blade aspect ratio A_{rat}. Four values of blade aspect ratio are examined: 1.00, 1.15, 1.30 and 1.48. The value $A_{rat} = 1.48$ corresponds to the INDUS compressor stage. Each data symbol on Figure 4-8 corresponds to a Monte Carlo simulation of 1000 trials.

Figures 4-9a and 4-9b indicate that the mean pressure rise and the mean efficiency increase with the aspect ratio over the range shown. Figures 4-9e and 4-9f indicate that the coefficients of variability decrease when the blade aspect ratio increases. Figures 4-9c and 4-9d show that the mean decrease in pressure rise and efficiency is higher when the blade aspect ratio is lower.

4.4 Comparison With Other Information About Variability

4.4.1 The One-Dimensional Model of Garzon

As mentioned in Section 2.6, Garzon [6] documented the impact of geometric variability on compressor pressure ratio and polytropic efficiency for a six-stage axial compressor. His algorithm was modified to record the performance of the first stage STAGE1, using the

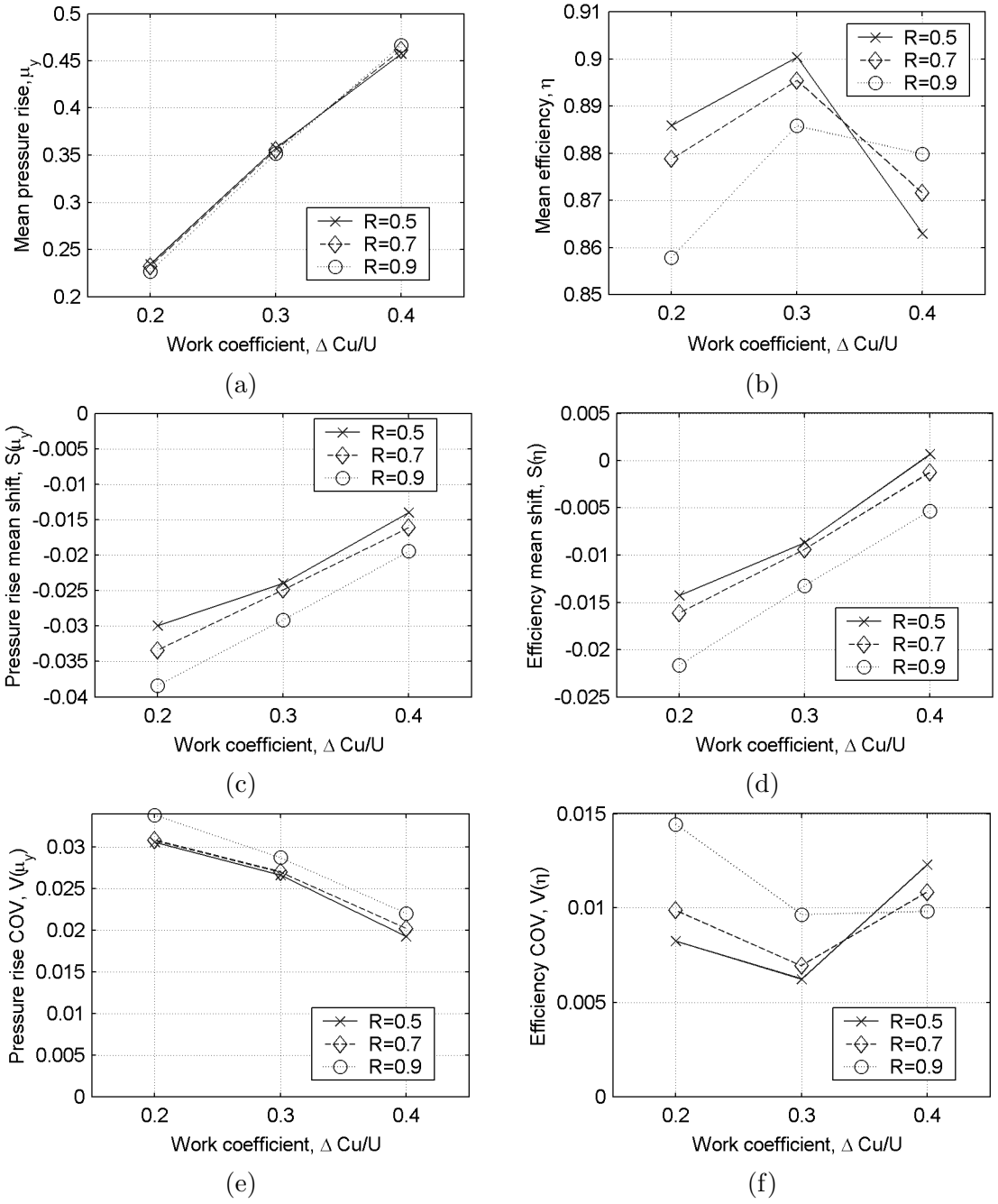

Figure 4-8: Performance of variants of the INDUS compressor, computed using Monte Carlo simulation at design incidence. Compressors differ in work coefficient $\frac{C_{u2}-C_{u1}}{U}$ and degree of reaction R.

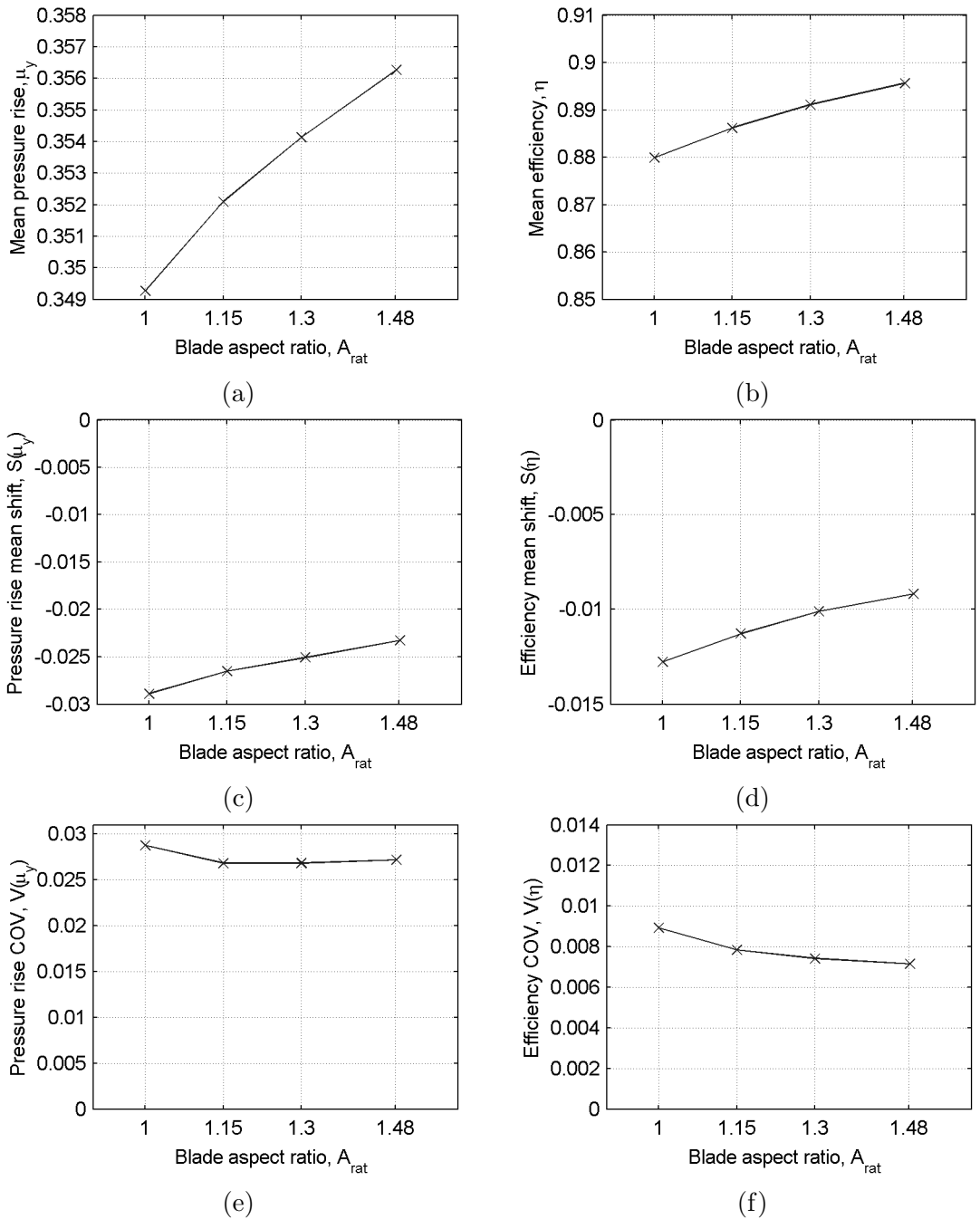

Figure 4-9: Performance of variants of the INDUS compressor, computed using Monte Carlo simulation at design incidence. Compressors differ in blade aspect ratio A_{rat}. Physical tip clearances and blade profiles are maintained the same.

Values	*Pressure ratio* π	*Polytropic efficiency* η
Nominal value	1.655 (1.104)	0.966 (0.904)
Mean value $\hat{\mu}$	1.619 (1.076)	0.954 (0.896)
Standard deviation $100 \cdot \hat{\sigma}$	3.4 (4.3)	0.703 (0.618)
Mean shift $100 \cdot \hat{S}$	-2.1 (-2.5)	-1.12 (-0.94)
Coefficient of variability $100 \cdot \hat{V}$	2.12 (2.63)	0.74 (0.69)

Table 4.4: Statistical results of the Monte Carlo analysis using the mean-line algorithm of Garzon on the STAGE1 compressor at design incidence. Figures in parentheses correspond to the INDUS compressor analyzed with the mean-line method developed in this thesis.

same geometry and inlet conditions. His method does not account for end-wall effects and tip clearance variability. A Monte Carlo simulation with 10000 trials was conducted at design incidence. Results are reported in Table 4.4, along with the results obtained for the INDUS compressor stage using the method developed in this thesis.

Table 4.4 shows that performance sensitivity for STAGE1 is in accord with results for INDUS. Mean shifts for pressure are close (-2.1% vs. -2.5%), mean shift for efficiency is a little higher for STAGE1 (-1.12% vs. -0.94%). This agreement is not surprising: Table 4.3 shows that tip clearances do not modify the mean shifts for pressure rise and efficiency. The 0.74% coefficient of variability for STAGE1 efficiency is close to the 0.69% coefficient for INDUS. The 2.12% coefficient of variability for STAGE1 pressure ratio is smaller than the 2.63% coefficient for INDUS. This is seen as the effect of tip clearances, which are the second source of variability according to Table 4.3.

4.4.2 The Mean-Line Model of Lavainne

Lavainne [12] characterized geometric variability using a quasi-3D mean-line model based on MISES coupled with end-wall correlations. His results were for transonic Mach numbers. He examined changes in chord, maximum thickness, and leading and trailing edge angle and thickness, whereas the present work relates geometric variability to variations in turning and losses. Time considerations did not allow him to conduct a Monte Carlo analysis directly with the mean-line model. Instead, he carried out a probabilistic analysis from a quadratic surface response based on 57 trials. To compare performance, he kept constant the ratio of pressure rise to mass flow (fixed operating line), whereas the present work keeps constant the incidence angle. The distribution of Lavainne for tip clearances was not symmetric. He found that he needed to consider a blockage change across the rotor, i.e. within the stage. This is not included in the present model.

Results for the mean-line analysis carried out by Lavainne on the third stage of the CREATE compressor are reported in Table 4.5. The shifts in pressure ratio and efficiency in the absence of the variability of one parameter are non-dimensionalized using the case where all sources of variability are accounted for. This allows comparing the relative importance of each variable on the degradation of performance. A Monte Carlo simulation of the INDUS stage is also conducted using the model developed in this thesis, and results are reported in Table 4.6.

Figures for the mean shift in efficiency are comparable: Lavainne reported a decrease of 0.59 points at fixed ratio of pressure ratio to mass flow, this work indicates a 0.85

Geometric parameter	$100 \cdot (\hat{\mu}_\pi - \pi^*)$	$100 \cdot \hat{\sigma}_\pi$	$100 \cdot (\hat{\mu}_\eta - \eta^*)$	$100 \cdot \hat{\sigma}_\eta$
All applied	-0.360	0.968	-0.590	1.156
Var. NOT applied	$\frac{\hat{\mu}_{\pi_i} - \hat{\mu}_\pi}{\pi^* - \hat{\mu}_\pi}$	$\frac{\hat{V}_{\pi_i}}{\hat{V}_\pi}$	$\frac{\hat{\mu}_{\eta_i} - \hat{\mu}_\eta}{\eta^* - \hat{\mu}_\eta}$	$\frac{\hat{V}_{\eta_i}}{\hat{V}_\eta}$
Rotor tip clearance ϵ_r	0.00	0.12	0.03	0.18
Stator tip clearance ϵ_s	0.05	0.03	0.07	0.13
Tip clearances ϵ_r, ϵ_s	0.06	0.16	0.10	0.34
Rotor chord c_r	0.00	0.00	0.04	0.00
Stator chord c_s	0.01	0.00	0.02	0.00
Rotor LE Angle	0.50	0.30	0.35	0.11
Stator LE Angle	0.01	0.00	0.03	0.00
Rotor TE Angle	-0.01	0.02	0.07	0.07
Stator TE Angle	0.01	0.00	0.03	0.00
Rotor LE Thickness	0.31	0.01	0.18	0.01
Stator LE Thickness	0.00	0.00	0.05	0.00
Rotor TE Thickness	0.03	0.00	0.01	0.01
Stator TE Thickness	0.01	0.00	0.01	0.00
Rotor Max. Thick. t_r	0.08	0.07	0.15	0.01
Stator Max. Thick t_s	0.02	0.00	0.04	0.01

Table 4.5: Mean shift and variability of the Monte Carlo analysis on the response surface of the sensitivity analysis at design incidence, using the mean-line algorithm of Lavainne with the third stage of the CREATE compressor [12].

Geometric parameter	$100 \cdot \hat{S}_{all}(\mu_y)$	$100 \cdot \hat{V}_{all}(\mu_y)$	$100 \cdot \hat{S}_{all}(\eta)$	$100 \cdot \hat{V}_{all}(\eta)$
All applied	-2.48	2.63	-0.94	0.69
Var. NOT applied	$\frac{\hat{\mu}_{\mu_{y_i}} - \hat{\mu}_{\mu_y}}{\mu_y{}^* - \hat{\mu}_{\mu_y}}$	$\frac{\hat{V}_{\mu_{y_i}}}{\hat{V}_{\mu_y}}$	$\frac{\hat{\mu}_{\mu_{y_i}} - \hat{\mu}_{\mu_y}}{\mu_y{}^* - \hat{\mu}_{\mu_y}}$	$\frac{\hat{V}_{\mu_{y_i}}}{\hat{V}_{\mu_y}}$
Rotor tip clearance ϵ_r	0.00	0.02	0.03	0.15
Stator tip clearance ϵ_s	0.04	0.01	0.04	0.00
Tip clearances ϵ_r, ϵ_s	-0.02	0.03	0.03	0.19
Rotor losses ω_r	0.21	0.03	0.70	0.30
Stator losses ω_s	0.12	-0.02	0.36	0.06
Turning ϑ	0.63	0.74	0.02	0.00

Table 4.6: Mean shift and variability of the Monte Carlo analysis at design incidence, using the model detailed in this thesis with the INDUS compressor.

Geometric parameter	$100 \cdot (\hat{\mu}_\pi - \pi^*)$	$100 \cdot \hat{\sigma}_\pi$	$100 \cdot (\hat{\mu}_\eta - \eta^*)$	$100 \cdot \hat{\sigma}_\eta$
All applied	-0.41	1.8	-0.45	2.0
Var. NOT applied	$\frac{\hat{\mu}_{\pi_i} - \hat{\mu}_\pi}{\pi^* - \hat{\mu}_\pi}$	$\frac{\hat{V}_{\pi_i}}{\hat{V}_\pi}$	$\frac{\hat{\mu}_{\eta_i} - \hat{\mu}_\eta}{\eta^* - \hat{\mu}_\eta}$	$\frac{\hat{V}_{\eta_i}}{\hat{V}_\eta}$
Rotor tip clearance ϵ_r	0.63	0.72	0.58	0.75
Stator tip clearance ϵ_s	0.02	0.00	-0.01	0.01
Rotor chord c_r	0.00	0.00	0.01	0.00
Stator chord c_s	0.01	0.00	0.02	0.00
Rotor LE Angle	0.10	0.01	0.14	0.02
Stator LE Angle	0.02	0.00	0.04	0.00
Rotor TE Angle	0.05	0.03	0.04	0.00
Stator TE Angle	0.00	0.00	0.00	0.00
Rotor LE Thickness	0.06	0.00	0.08	0.00
Stator LE Thickness	0.02	0.00	0.04	0.00
Rotor TE Thickness	0.03	0.01	0.02	0.00
Stator TE Thickness	0.00	0.00	0.00	0.00
Rotor Max. Thick. t_r	0.04	0.00	0.03	0.00
Stator Max. Thick t_s	0.01	0.00	0.02	0.00

Table 4.7: Mean shift and variability of the Monte Carlo analysis on the response surface of the sensitivity analysis at design incidence, using the 3D algorithm of Lavainne with the third stage of the CREATE compressor [12].

point decrease at fixed design incidence. In both cases, pressure rise and efficiency are impacted substantially by $\pm 2\sigma$ values of tip clearance, but tip clearance has a small effect on pressure rise and efficiency mean shift. The contributions of tip clearance compared to other geometric parameters to pressure rise and efficiency coefficients of variability are also of the same magnitude. Lavainne reported a higher influence of tip clearance on mean performance: in absence of tip clearance variability, he observed a 16% and a 34% decrease in pressure rise and efficiency, to compare to with the 3% and 19% of this study.

4.4.3 The Three-Dimensional Model of Lavainne

Lavainne also carried out a probabilistic analysis based on a three-dimensional Reynolds Average Navier-Stokes solver. Results are reported in Table 4.7. This analysis indicated that 60% of the mean decrease in pressure ratio and efficiency were due to rotor tip clearance, while Table 4.6 shows negligible impact based on the mean-line method developed in this thesis. The 3D simulation attributes 75% of the variability in pressure ratio and efficiency to rotor tip clearance, while Table 4.6 indicates 15% for the mean-line method. Results for the mean-line method exposed in this thesis are thus roughly similar to the mean-line method of Lavainne which differed from his 3D simulation.

Chapter 5

Summary and Recommendations

5.1 Summary

A mean-line axial compressor repeating-stage model was developed from data available in the open literature. It includes correlations for deviation angles, profile losses, stalling static pressure rise and end-wall blockage. This algorithm was tested and validated for Mach number regimes characteristic of industrial compressors.

The model was used with a Monte Carlo process to assess probabilistically the impact of geometric variability on compressor performance. Blade profile variability was implemented by transforming the profile losses and rotor turning into random variables. Mean shifts and coefficients of variability were assumed to be the same as those of a reference rotor examined by Garzon [6]. Tip clearance variation was also included in the model, using a normal distribution for the variation.

At design incidence, geometric variability caused a 1% drop in polytropic efficiency mostly due to the mean shift in profile losses, and a 2.5% decrease in pressure rise mostly due to the mean shift in turning. The impact of the probabilistic component on mean performance is negligible compared to that due to the mean shift. In terms of mean shift, turning and rotor losses are the key factors, whereas the effects of tip clearance can be neglected. Turning variability accounts for the major part of the 2.5% pressure coefficient of variability, whereas tip clearance and losses contribute to a comparable extent to the 0.7% efficiency coefficient of variability. Contributions of rotor losses and tip clearance represent two times those of stator losses and tip clearance.

Overall results at design incidence are similar to the one-dimensional mean-line algorithm of Garzon, which does not include tip clearance and end-wall effects. Results for efficiency mean shift are compatible with a quasi-3D mean-line analysis carried out by Lavainne [12]. Although Lavainne observed on a compressor with lower aspect ratio that tip clearances were the key drivers for pressure rise and efficiency variability, they come second in rank in this study. A three-dimensional analysis using a Reynold Average Navier-Stokes solver conducted by Lavainne revealed a much larger effect of tip clearance on mean performance and variability. The difference is attributable to the repeating-stage model used for the end-wall flow.

The overall performance degrades approximately linearly with the fraction of the corrective mean shift effectively retained. A parametric study for different stage designs revealed less sensitivity to geometric variability in terms of mean shift and coefficient of variability for compressor stages with higher work coefficient and lower reaction. Changes in aspect

ratio were also examined over a limited range and it was found that there was a higher variability and a higher decrease in mean performance for stages with lower blade aspect ratio. However, the main difference between these results and those of Lavainne are thought to be not aspect ratio, but rather the inclusion of the end-wall displacement thickness change within the stage, an effect not taken into account by the present model.

5.2 Suggestions for Future Work

- End-wall blockage variation should be carried out on a row-by-row basis to assess effects of axial velocity ratio, which Lavainne [12] has found to be important.
- Further investigations are needed to account for the greater influence of tip clearance on pressure rise and efficiency variability reported by Lavainne [12]. In particular, the effect of blade aspect ratio needs to be clarified.
- The investigation of variation should be extended to a multi-stage configuration and to transonic conditions to assess the performance degradation of a whole compressor.
- The mean-line model should be replaced by a quasi-3D model to eliminate the intermediary representation of geometric variability as perturbations on profile losses and turning.

Appendix A

Repeating-Stage Implementation

A.1 Overall View

The CHARAX algorithm introduced in Section 3 is implemented as a Fortran 77 program. The programming language was chosen for the sake of simplicity, as the original routines of Casey were already written in Fortran. The source code is compiled using the GNU Fortran compiler (release 3.2), and input and output operations are limited to reading and writing of ASCII files. This increases the code portability, and allows a reduced computation time of 0.3 seconds per stage simulation on a personal computer equipped with a 2 GHz Pentium IV processor and with 512 Mo of RAM.

Figure A-1 shows an overall view of the modules at the base of the algorithm:

1. The INPUT module reads the `INPUT.TXT` file, and initializes most of the geometric parameters.
2. From these parameters, the ANALYS module determines the blade metal angles and design coefficients.
3. The results of ANALYS are printed using the PRINTA module.
4. The SETUP module processes these results to determine the last geometric parameters.
5. The modules SURGE, CHOKE and OPTIM allow positioning respectively the surge, choke and optimum points.
6. The CURVE module computes the characteristic curves for pressure rise, efficiency, and other significant parameters. It writes the results in files `OUTPUT.TXT` and `OUTPUT2.TXT`.

A.2 Initialization Tasks

A.2.1 Program Input and First Geometric Parameters

Here is a typical `INPUT.TXT` file and the corresponding parameter template:

```
0.710000,1.300000,1.000000
36,1.000000,0.088000,0.020400,0.003000
36,1.000000,0.080000,0.020400,0.003000
5.61,55.76,36.51,39.33
4.000000,0.450000
```

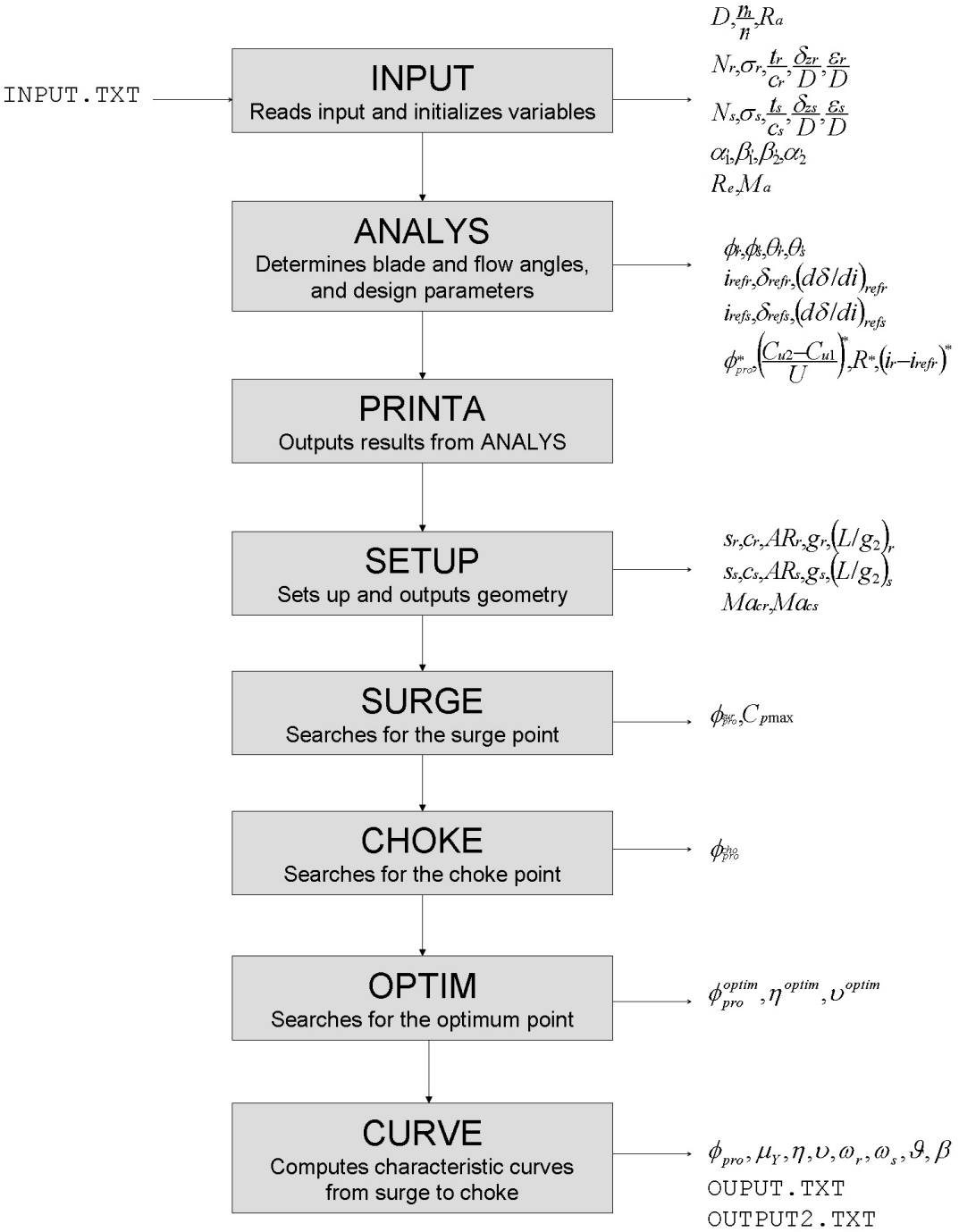

Figure A-1: Algorithm flow diagram

$$D, \frac{r_t}{r_h}, R_a$$
$$N_r, \sigma_r, \frac{t_r}{c_r}, \frac{\delta_{xr}}{D}, \frac{\epsilon_r}{D}$$
$$N_s, \sigma_s, \frac{t_s}{c_s}, \frac{\delta_{xs}}{D}, \frac{\epsilon_s}{D}$$
$$\alpha_1{}', \beta_1{}', \beta_2{}', \alpha_2{}'$$
$$R_e, M_a$$

After reading the `INPUT.TXT` file, the INPUT module computes the geometric parameters as follows. As the stage is assumed to keep constant hub and tip radii along the compressor axis, the hub diameter D (expressed in meters) and the tip to hub radius ratio $\frac{r_t}{r_h}$ completely define the stage geometry. Knowing them, it is straightforward to compute the annulus height h, the r.m.s. radius r_{rms}, and the blade velocity at the hub U_h:

$$h = \frac{D\left(\frac{r_t}{r_h} - 1\right)}{2},$$

$$r_{rms} = \frac{1}{2} D \sqrt{\frac{\left(\frac{r_t}{r_h}\right)^2 + 1}{2}},$$

$$U_h = \frac{U}{\sqrt{\frac{\left(\frac{r_t}{r_h}\right)^2 + 1}{2}}}.$$

It is convenient to introduce the r.m.s. radius factor, λ, defined as:

$$\lambda = \sqrt{\frac{\left(\frac{r_t}{r_h}\right)^2 + 1}{2}}.$$

The center-line average roughness R_a read from the `INPUT.TXT` file is multiplied by 10^{-6}. In the same way, the value of the Reynolds number R_e is multiplied by 10^6. Knowing the number of rotor and stator blades N_r and N_s, the computation of the circumferential spacing between two blades at the r.m.s. radius is immediate:

$$s_r = \frac{2\pi r_{rms}}{N_r}, s_s = \frac{2\pi r_{rms}}{N_s}.$$

From the blade solidity σ_r and σ_s, the blade chords at r.m.s. radius c_r and c_s can be determined:

$$c_r = \sigma_r \cdot s_r, c_s = \sigma_s \cdot s_s.$$

Rotor blade thickness, axial spacing and tip clearance are given as ratios with D and c. The metal angles $\alpha_1{}'$, $\alpha_2{}'$, $\beta_1{}'$ and $\beta_2{}'$ are expressed in degrees. The usual definition for the blade aspect ratio A_{rat} is retained, and it can be written as:

$$A_{rat} = \frac{h}{c}.$$

A.2.2 Reference Deviation and Incidence Angles

The ANALYS module determines for both rotor and stator:

- the reference incidence angle i_{ref};
- the deviation angle at the reference incidence angle δ_{ref};
- a linear correlation coefficient $(d\delta/di)_{ref}$.

The deviation angle is computed as follows:

$$\delta_r = \delta_{refr} + (d\delta/di)_{refr} \cdot (i_r - i_{refr}).$$

i_{ref} is computed in an iterative procedure made of equations originally introduced by Lieblein [14]. A description of the process for the rotor follows, but the same reasoning applies for the stator. The only input parameters necessary to compute i_{refr} are ${\beta_1}'$, ${\beta_2}'$, t_r and σ_r, which are read from the input file. The iterative loop is initialized with $i_{ref} = 0$:

$$\begin{aligned} \beta_1 &= {\beta_1}' + i_{refr} \\ i_0 &= FI010\,(\beta_1, \sigma_r) \cdot DIDT\,(t_r) \\ n_r &= DIDFI\,(\beta_1, \sigma_r) \\ i_{refr} &= i_0 + n_r {\phi'}_r - 1. \end{aligned}$$

Finally, δ_{ref} is computed using a variant of Carter's rule proposed by Davis [4], whereas $(d\delta/di)_{ref}$ is computed from the data of Lieblein using equations given by Crouse [3]:

$$\delta_{refr} = \left(0.216 + 0.000972 \cdot {\theta'}_r + 0.0000238 \cdot {\theta'}_r{}^2\right) \frac{{\phi'}_r}{\sigma_r}$$

$$(d\delta/di)_{refr} = DDDDI\,(\beta_1, \sigma_r)\,.$$

A.2.3 From Metal Angles to Design Coefficients

When $\phi_{pro} = {\phi_{pro}}^*$, the rotor and stator losses are minimum, this is therefore the desired point of operation and it is important to know it precisely. When metal angles are used as an input for the algorithm, the design two-dimensional flow coefficient ${\phi_{pro}}^*$ is computed in the ANALYS module as follows:

1. Initialize ${\phi_{pro}}^*$ as $\frac{1}{\tan {\alpha_1}' + \tan {\beta_1}'}$.
2. Resolve the velocity triangles as indicated in A.3.2.
3. Determine a mean incidence level $i_{rs} = \frac{1}{2}\,(i_r - i_{refr} + i_s - i_{refs})$.
4. Determine the air angles with a reduced incidence:

$$\begin{cases} \alpha_1 := \alpha_1 - i_{rs} \cdot (d\delta/di)_{refs} \\ \beta_1 := \beta_1 - i_{rs} \\ \beta_2 := \beta_2 - i_{rs} \cdot (d\delta/di)_{refr} \\ \alpha_2 := \alpha_2 - i_{rs}. \end{cases}$$

5. Compute the new value ${\phi_{pro}}^* := \frac{1}{\tan\alpha_1 + \tan\beta_1}$. Reiterate steps 2, 3, 4 and 5 until ${\phi_{pro}}^*$ converges.

Knowing ${\phi_{pro}}^*$, the resolution of the velocity triangles directly yields the design values for the work coefficient $\left(\frac{C_{u2}-C_{u1}}{U}\right)^*$, the degree of reaction R^* and the incidence difference $(i_r - i_{refr})^*$. Variables ${\phi_{pro}}^*$, $\left(\frac{C_{u2}-C_{u1}}{U}\right)^*$, R^* and $(i_r - i_{refr})^*$ are called the design coefficients.

A.2.4 From Design Coefficients to Metal Angles

Instead of imposing the metal angles ${\alpha_1}'$, ${\alpha_2}'$, ${\beta_1}'$ and ${\beta_2}'$, it is often more convenient to impose as an input the nominal values for the two-dimensional flow coefficient ${\phi_{pro}}^*$, the work coefficient $\left(\frac{C_{u2}-C_{u1}}{U}\right)^*$, the degree of reaction R^* and the incidence angle difference $(i_r - i_{refr})^*$. Formally, both formulations are equivalent. In that case, the DESIGN module replaces the ANALYS module. From ${\phi_{pro}}^*$, R^*, $\left(\frac{C_{u2}-C_{u1}}{U}\right)^*$ and $(i_r - i_{refr})^*$, the DESIGN module determines the air angles at design:

$$\begin{cases} \alpha_1 := \arctan\left(\frac{1}{{\phi_{pro}}^*} \cdot \left((1-R^*) - \frac{1}{2}\left(\frac{C_{u2}-C_{u1}}{U}\right)^*\right)\right) \\ \alpha_2 := \arctan\left(\frac{1}{{\phi_{pro}}^*} \cdot \left((1-R^*) + \frac{1}{2}\left(\frac{C_{u2}-C_{u1}}{U}\right)^*\right)\right) \\ \beta_1 := \arctan\left(\frac{1}{{\phi_{pro}}^*} \cdot \left(R^* + \frac{2}{2}\left(\frac{C_{u2}-C_{u1}}{U}\right)^*\right)\right) \\ \beta_2 := \arctan\left(\frac{1}{{\phi_{pro}}^*} \cdot \left(R^* - \frac{2}{2}\left(\frac{C_{u2}-C_{u1}}{U}\right)^*\right)\right). \end{cases}$$

The computation of the reference incidence and deviation angles described in A.2.2 must then be adapted, but the iteration process and the correlations involved are basically the same, and allow determining i_{ref}, δ_{ref} and $(d\delta/di)_{ref}$ for both rotor and stator. The design deviation angles are then computed using:

$$\begin{cases} \delta_r := \delta_{refr} + (d\delta/di)_{refr} \cdot (i_r - i_{refr})^* \\ \delta_s := \delta_{refs} - (d\delta/di)_{refs} \cdot (i_r - i_{refr})^*. \end{cases}$$

The metal angles are derived from the following equations:

$$\begin{cases} {\alpha_1}' := \alpha_1 - \delta_s \\ {\beta_1}' := \beta_1 - i_r \\ {\beta_2}' := \beta_2 - \delta_r \\ {\alpha_2}' := \alpha_2 - i_s. \end{cases}$$

The knowledge of the design coefficients is therefore equivalent to the knowledge of the metal angles.

A.2.5 Other Fixed Parameters

At this point, the metal angles and the design coefficients are fully determined, so that the SETUP module can compute the last geometric parameters. From Figure 3-2, it is straightforward to see that the blade staggered spacing for the rotor g_r can be computed as:

$$g_r = s_r \cdot \cos{\theta'}_r.$$

The mean-line arc-length of a circular airfoil can be expressed for the rotor as:

$$L = c_r \frac{\frac{\phi'_r}{2}}{\sin\left(\frac{\phi'_r}{2}\right)}.$$

The ratio of arc-length to cascade trailing edge staggered spacing $\frac{L}{g_2}$ is:

$$\frac{L}{g_{2\,r}} = \frac{L}{s_r \cdot \cos {\alpha_1}'}.$$

Jansen and Moffat [8] introduced a critical Mach number M_{ac}, used in the profile loss correlations. M_{ac} is computed from design values, and takes the following form for the rotor:

$$M_{acr} = f\left(\frac{t}{c}, \sigma, C_{u2} - C_{u1}, W_1, \gamma\right).$$

A.2.6 Expression of Inlet Conditions as Input Coefficients

In Section 3.4.1, the inlet conditions were defined by the Reynolds number R_e and the spool Mach number M_a. Adding to the definitions of R_e and M_a the ideal gas law and the formula of Sutherland for the dynamic viscosity, the following set of equations can be obtained:

$$\begin{cases} M_a = \frac{U_h}{\sqrt{\gamma R_b T}} \\ R_e = \frac{\rho U_h D}{\mu} \\ \frac{p}{\rho} = R_b T \\ \mu = 1.7894 \cdot 10^{-5} \frac{\left(\frac{T}{288.16}\right)^{\frac{3}{2}} (288.16+110)}{T+110}. \end{cases}$$

In practice, D and U_h are fixed parameters. The variables ρ and μ depend directly on the inlet pressure p and temperature T. When the temperature and pressure are set, the Reynolds and Mach numbers are fully determined as soon as either of them is assigned a value. The values for the Reynolds and Mach numbers chosen in Section 3.4.1 correspond, among other possibilities, to the following inlet conditions:

$$U_h = 32m/s, T_1 = 500K, p_1 = 10^5 Pa.$$

A.3 Main Program Loop

A.3.1 Flow Chart

Figure A-2 details the different steps of the CURVE module, which is the main algorithm routine:

1. A value for the two-dimensional flow coefficient ϕ_{pro} is chosen. All other values depend on this choice.
2. The velocity triangles are resolved for this value of ϕ_{pro} in the TRIANG module.
3. The ETASTA module determines the profile and end-wall losses, which depend on the current value of Ω. This yields the efficiency η and the end-wall boundary layer δ^*.

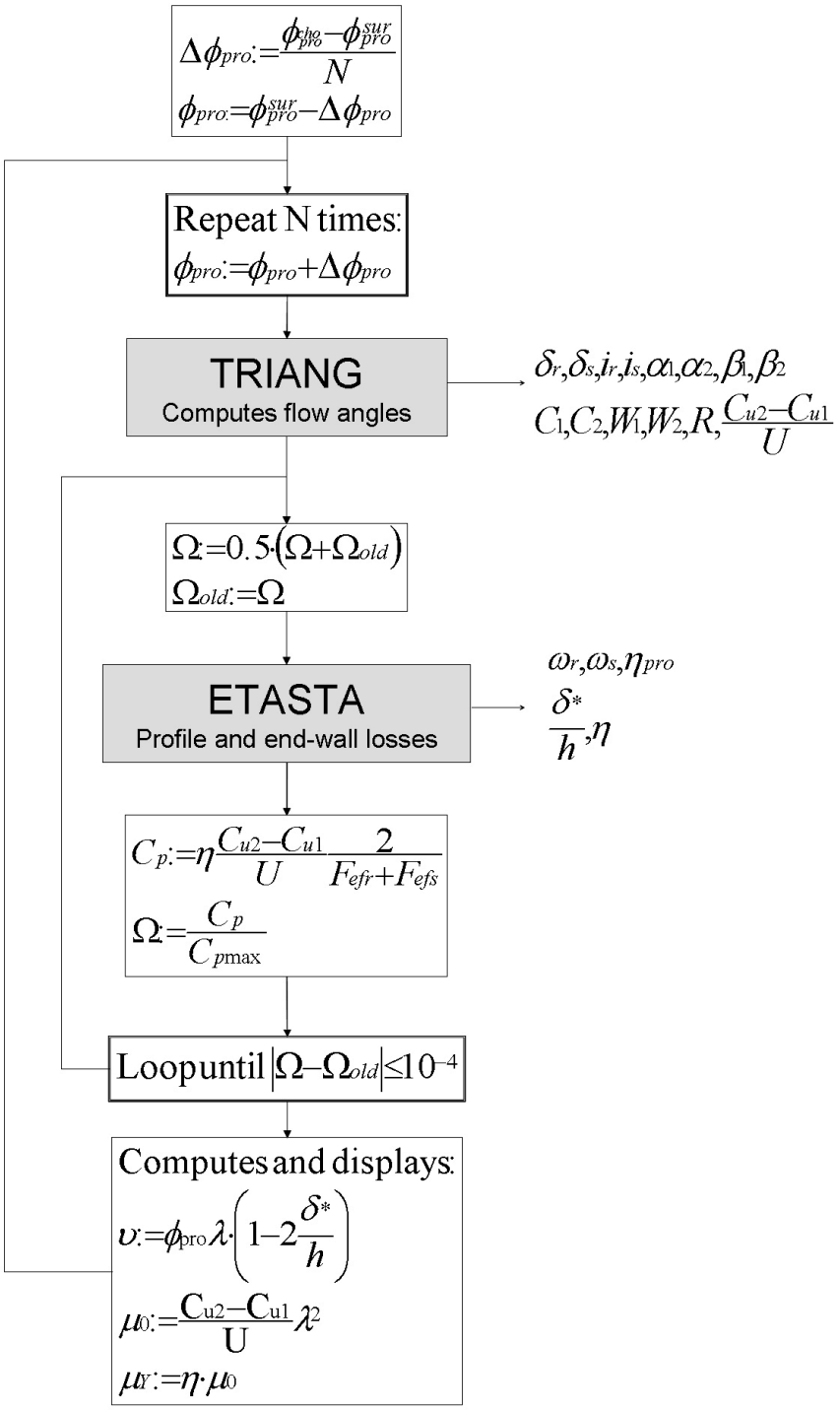

Figure A-2: Curve module

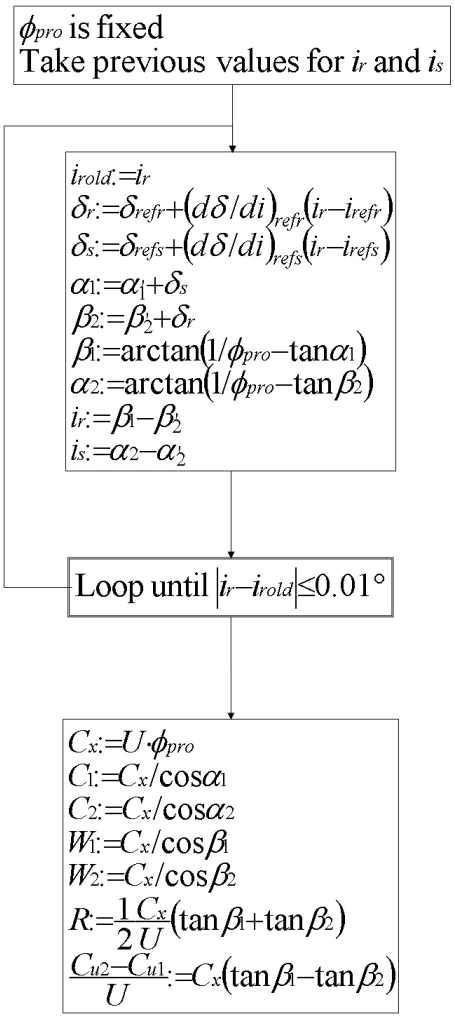

Figure A-3: Velocity triangle resolution module

4. The value of Ω is actualized, and steps 2 to 4 are iterated until convergence of Ω occurs.

5. When Ω is converged, the hub flow coefficient with end-walls ν and the pressure rise μ_y can be determined.

The details of each step will be addressed in the following sections.

A.3.2 Resolution of Velocity Triangles

Once the two-dimensional flow coefficient ϕ_{pro} is fixed, flow angles can be completely determined in the TRIANG module by an iterative loop where the incidence and deviation angles are taken into account. Convergence of i_r is used as a criterion for convergence of the whole

loop:

$$\begin{aligned}
\delta_r &:= \delta_{refr} + (d\delta/di)_{refr} \cdot (i_r - i_{refr}) \\
\delta_s &:= \delta_{refs} + (d\delta/di)_{refs} \cdot (i_r - i_{refs}) \\
\alpha_1 &:= \alpha_1{}' + \delta_s \\
\beta_2 &:= \beta_2{}' + \delta_r \\
\beta_1 &:= \arctan\left(1/\phi_{pro} - \tan\alpha_1\right) \\
\alpha_2 &:= \arctan\left(1/\phi_{pro} - \tan\beta_2\right) \\
i_r &:= \beta_1 - \beta_2{}' \\
i_s &:= \alpha_2 - \alpha_2{}'.
\end{aligned}$$

At the end of the iteration process, the incidence, deviation and incidence angles are known. It is then straightforward to compute the velocities, degree of reaction R and work coefficient $C_{u2} - C_{u1}$.

$$\begin{aligned}
C_1 &:= \frac{C_x}{\cos\alpha_1} \\
C_2 &:= \frac{C_x}{\cos\alpha_2} \\
W_1 &:= \frac{C_x}{\cos\beta_1} \\
W_2 &:= \frac{C_x}{\cos\beta_2} \\
R &:= \frac{1}{2}\frac{C_x}{U}\left(\tan\beta_1 + \tan\beta_2\right) \\
C_{u2} - C_{u1} &:= C_x\left(\tan\beta_1 - \tan\beta_2\right)
\end{aligned}$$

Figure A-3 illustrates this procedure. Before the pressure rise can be determined from the work coefficient, profile and end-wall losses must be accounted for.

A.3.3 Profile Losses

The rotor and stator profile pressure loss coefficients are defined as follows:

$$\begin{cases}
\omega_r = \frac{p_{T2} - p_{T1}}{\frac{1}{2}\rho_1 {W_1}^2} \\
\omega_s = \frac{p_{T3} - p_{T2}}{\frac{1}{2}\rho_2 {C_2}^2}.
\end{cases}$$

The ETASTA module computes the pressure profile loss coefficient for both rotor and stator as an incompressible coefficient corrected by three factors:

$$\omega = \omega_i \left(\omega/\omega_i\right)_{Re} \left(\omega/\omega_i\right)_{inc} \left(\omega/\omega_i\right)_{Ma},$$

where

- ω_i is the incompressible total pressure loss coefficient of the blade profile at the r.m.s.

radius and at the reference angle, computed following Lieblein [13]:

$$\omega_{ri} = OMEGAL(\beta_1{}' + i_{refr}, \beta_2{}' + \delta_{refr}, \sigma_r).$$

- $(\omega/\omega_i)_{Re}$ is the correction for Reynolds number, computed according to Koch [11]:

$$(\omega/\omega_i)_{Rer} = CORREN\left(\frac{\rho_1 c_r W_1}{\mu}, \frac{R_a}{c_r}\right).$$

- $(\omega/\omega_i)_{Ma}$ is the correction for Mach number as computed by Jansen and Moffat [8]:

$$(\omega/\omega_i)_{Mar} = CORMAC\left(M_{acr}, M_a W_1 \sqrt{\frac{\left(\frac{r_t}{r_h}\right)^2 + 1}{2}}\right).$$

- $(\omega/\omega_i)_{inc}$ is the correction for incidence, as defined in [8]:

$$(\omega/\omega_i)_{incr} = CORINC(\beta_1, \beta_1{}' + i_{refr}, \beta_2{}' + \delta_{refr}, \sigma_r, M_a, \delta\beta).$$

  The computation of $(\omega/\omega_i)_{inc}$ depends on the cascade operating range $\delta\beta$. The latter is defined as the range of inlet flow angle within which the loss coefficient is less than twice the minimum loss value:

$$\delta\beta = \delta\beta\left(\beta_1, \beta_2, \sigma, M_a\right).$$

This allows computing the profile efficiency:

$$\eta_{pro} = 1 - \frac{\omega_r {W_1}^2 + \omega_s {C_2}^2}{2U\left(C_{u2} - C_{u1}\right)}.$$

To compute the actual stage efficiency, end-wall losses must be accounted for.

A.3.4 End-Wall Losses

The losses due to leakage through the tip clearance of the blades, secondary flows and the end-wall boundary layers are calculated in the ETASTA module using a method proposed by Koch and Smith [11]. In this model, the stage efficiency in a repeating stage is calculated as:

$$\eta = \eta_{pro} \frac{1 - 2\frac{\delta^*}{h}}{1 - 2\frac{\tau}{h}},$$

where

- δ^* is the mean displacement thickness of the boundary layer;
- τ is the mean tangential-force thickness at the end-wall boundary layers.

Koch and Smith provided the following correlations for the values of δ^* and τ in terms of tip clearance and stage loading ratio:

$$\begin{array}{lcl} \frac{\delta^*}{h} & = & \frac{\delta^*}{g}\frac{\overline{g}}{h} \\ \frac{\delta^*}{g} & = & \left(\frac{\delta^*}{g}\right)_{\epsilon=0} + \Omega\frac{\overline{\epsilon}}{g} \\ \left(\frac{\delta^*}{g}\right)_{\epsilon=0} & = & f_1(\Omega) \\ \frac{\tau}{h} & = & \frac{\tau}{\delta^*}\frac{\delta^*}{h} \\ \frac{\tau}{\delta^*} & = & f_2(\Omega), \end{array}$$

where

- $\frac{\overline{g}}{h}$ is the ratio of stage average staggered spacing to annulus height, defined as:

$$\frac{\overline{g}}{h} = \frac{{W_1}^2\frac{g_r}{h} + {C_2}^2\frac{g_s}{h}}{{W_1}^2 + {C_2}^2}.$$

- $\left(\frac{\delta^*}{g}\right)_{\epsilon=0}$ is the ratio of displacement thickness to staggered spacing with zero tip clearance.

- Ω is the ratio of static pressure rise coefficient to stalling static pressure rise coefficient, also called stage loading ratio.

- $\frac{\overline{\epsilon}}{g}$ is the ratio of stage–average to clearance–staggered spacing, defined as:

$$\frac{\overline{\epsilon}}{g} = \frac{{W_1}^2\frac{\epsilon_r}{g_r} + {C_2}^2\frac{\epsilon_s}{g_s}}{{W_1}^2 + {C_2}^2}.$$

- the functions f_1 and f_2 are correlations extracted from [11], and illustrated in Figure 2-2.

The displacement thicknesses predicted by the above equations are used to compute the actual flow coefficient ϕ of the stage from the free-stream flow coefficient ϕ_{pro} by taking into account the blockage as follows:

$$\phi = \phi_{pro} \cdot \left(1 - 2\frac{\delta^*}{h}\right).$$

The hub flow coefficient ν can then be determined using:

$$\nu = \lambda \cdot \phi.$$

A.3.5 Stalling Static Pressure Rise Coefficient and Stage Loading Ratio

The stage loading ratio Ω mentioned in Section 3.4.2 is computed as the ratio of the static pressure rise coefficient C_p with the stalling static pressure rise coefficient $C_{p_{max}}$:

$$\Omega = \frac{C_p}{C_{p_{max}}}.$$

While C_p is computed for each iteration, $C_{p_{max}}$ is computed once when the surge point in determined.

In the computation of the stage loading ratio, the stage static pressure rise coefficient C_p is corrected by the effective dynamic pressure factor $\mathcal{F}_{ef}$ defined by Koch in [10], to account for inlet skew:

$$C_p = \eta \frac{C_{u2} - C_{u1}}{U} \frac{2}{\mathcal{F}_{ef_r} + \mathcal{F}_{ef_s}}.$$

A.4 Determination of Characteristic Points

As mentioned in Section A.1, the surge, choke and optimum points are determined before computing the characteristic curve to know in advance which range of the two-dimensional flow coefficient ϕ_{pro} to explore. However, as the routines are entirely based on the program main loop, it is convenient to introduce them here.

A.4.1 Surge Point

As illustrated in Figure A-4, the SURGE module is similar to the CURVE module. The main difference is the addition of the CHMAX module that computes the maximum value of the static pressure rise coefficient $C_{p_{max}}$. An outer loop tests a range of possible values for the surge flow coefficient. This loop converges when $\Omega = 1$. An inner loop converges with any given value of Ω. For a given value of the flow coefficient ϕ_{pro} and of the stage loading ratio Ω, profile and end–wall losses are computed to determine the stage efficiency η. Values for C_p and $C_{p_{max}}$ are then determined, which yields a new value for Ω.

In the CHMAX module, $C_{p_{max}}$ is calculated following Koch [10] as:

$$C_{p_{max}} = C_{p_D} \left(C_p/C_{p_D}\right)_{Re} \left(C_p/C_{p_D}\right)_{\epsilon} \left(C_p/C_{p_D}\right)_{\Delta z},$$

where

- C_{p_D} is the maximum static pressure rise coefficient from the corrected diffuser correlation, with:
$$C_{p_D} = C_{p_{2D}} - 0.02 \frac{{W_1}^2 \frac{L}{g_2}_r + {C_2}^2 \frac{L}{g_2}_s}{{W_1}^2 + {C_2}^2},$$
where C_{p_D} is illustrated in Figure 2-3.
- $\left(C_p/C_{p_D}\right)_{Re}$ is the Reynolds number correction, where W_1 and C_2 intervene.
- $\left(C_p/C_{p_D}\right)_{\epsilon}$ is the tip clearance correction.
- $\left(C_p/C_{p_D}\right)_{\Delta z}$ is the axial spacing correction.

A precise determination of the surge point is critical: it allows the simultaneous computation of the surge flow coefficient ϕ_{pro_s} and of the maximum pressure rise $C_{p_{max}}$.

The operating range mentioned in Section A.3.3 is used as a second way to determine the surge when the incidence reaches a threshold maximum value. Stall is assumed to occur due to leading edge incidence effects if at the r.m.s. radius:

$$i - i_{ref} = 0.8 \frac{\delta\beta}{2}.$$

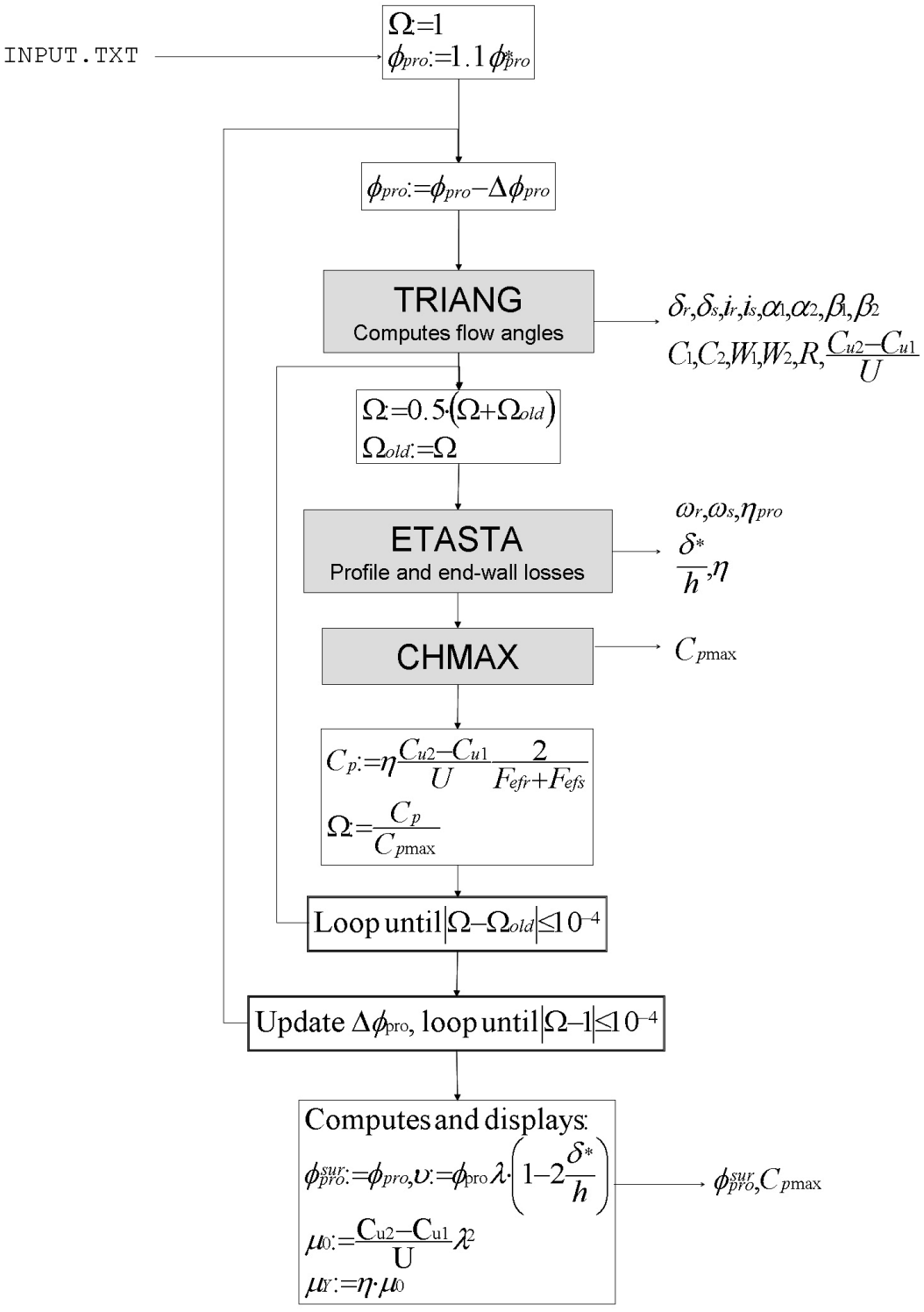

Figure A-4: Surge module

A.4.2 Choke Point

The CURVE module knows which minimum value of ϕ_{pro} to consider thanks to the SURGE module, and in the same way, it knows the maximum value of ϕ_{pro} to consider thanks to the CHOKE module. As Figure A-5 shows it, the choke point is sought as being the position where the stage loading ratio is null. This corresponds to the point of null pressure rise.

A.5 Output Files

The program produces two ASCII files. `OUTPUT.TXT` contains information about the geometry and the computation process. `OUTPUT2.TXT` contains only the characteristic curves, and is used by the probabilistic algorithm.

A.5.1 OUTPUT.TXT

```
     AXIAL COMPRESSOR STAGE  CHARACTERISTIC PROGRAM :  CHARAX
      ================================================      Vers. mV01

     LISTING OF INPUT DATA
     ---------------------
 MATLAB ROUTINE
 CF ORIGINAL
     0   50
     0    0    0    0    0    0
    0.71000   1.30000   1.00000
    36   1.00000   0.08800   0.02040   0.00300
    36   1.00000   0.08000   0.02040   0.00300
      0.600     0.300     0.700     0.000
      4.000     0.450
    1.00000   1.00000   1.00000


     DESIGN VERSION  OF PROGRAM (IDEA =  0)


     CORRECTION FACTORS F1  F2  F3 =   1.000    1.000    1.000


     BLADE AND FLOW ANGLES

     ALFA1  =   14.04   BETA1   =  54.78   BETA2  =  42.51   ALFA2   =   36.87
     ALFA1S =   5.61   BETA1S  =   55.76   BETA2S =  36.51   ALFA2S  =   39.33
     SDREF  =   8.43   RIREF   =   -0.98   RDREF  =   6.00   SIREF   =   -2.46
     FIRS   =  19.25   THETRS  =   46.14   FISS   =  33.72   THETSS  =   22.47


     PROFILE VELOCITY TRIANGLE DESIGN  PARAMETERS

     CXD =  0.600   DCUD =  0.300   DRD =  0.700
     (I-Iref)r =    0.00   (I-Iref)s =     0.00


     STAGE GEOMETRY

     DN =  0.710  YT =  1.300  Yrms  =  1.160  H =   0.106  Ra =  0.100E-05
```

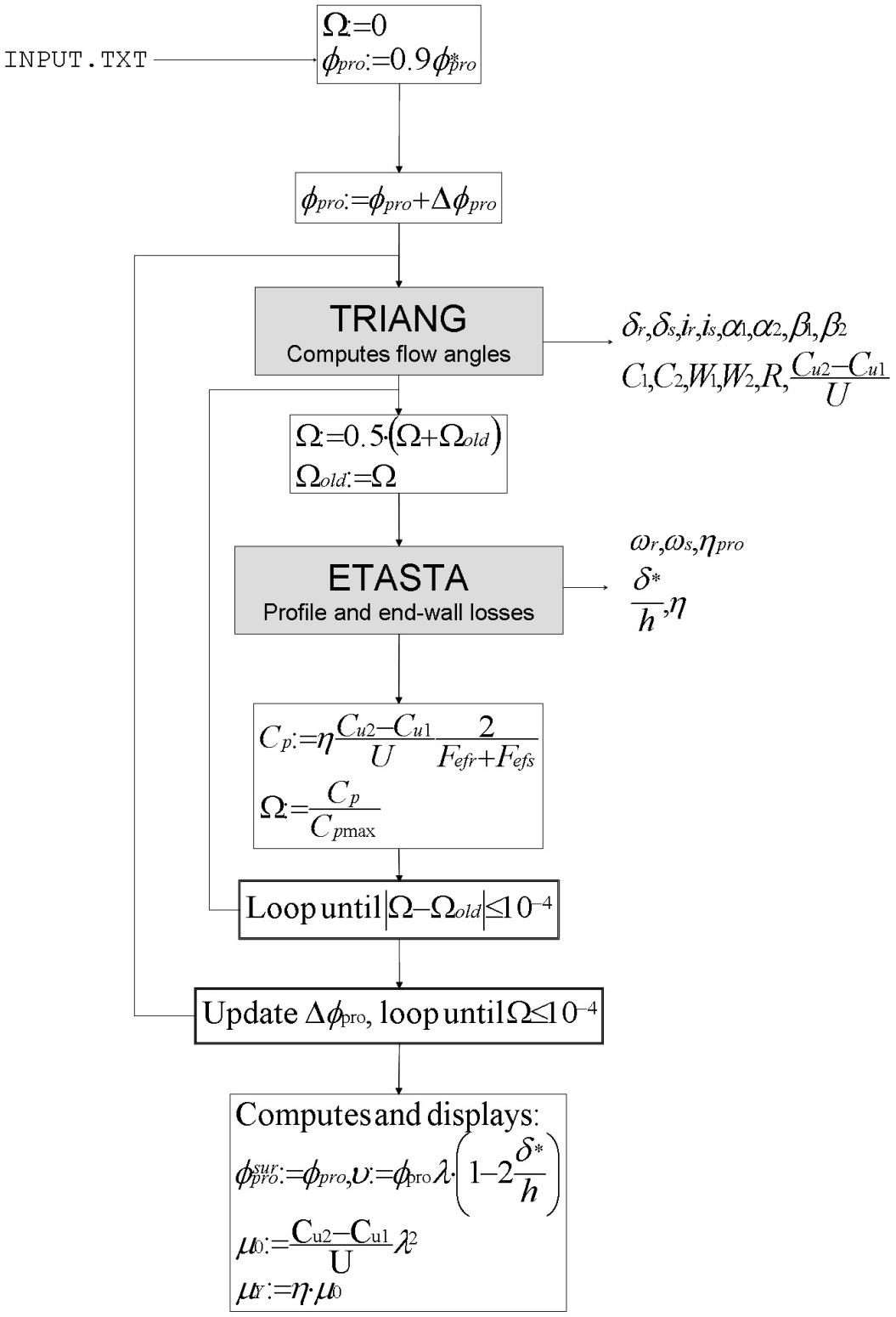

Figure A-5: Choke module

```
ROTOR GEOMETRY

NZ  =  36  S  =   0.072  SIGMA =  1.000  C =  0.072  AR =   1.482
T/C =  0.088  CL = 0.0030  DZ  =  0.020  G =   0.050   L/G2 =  1.250
Ra/C =   0.139E-04   CDmin =   0.00419
DELBETAi =  9.233   MAcr  =   0.749   DD/DI =  0.09241


STATOR  GEOMETRY

NZ  =  36  S  =   0.072  SIGMA =  1.000  C =  0.072  AR =   1.482
T/C =  0.080  CL = 0.0030  DZ  =  0.020  G =   0.066   L/G2 =  1.019
Ra/C =   0.139E-04   CDmin =   0.00419
DELBETAi = 11.509   MAcr  =   0.715   DD/DI =  0.06231


AERODYNAMIC PARAMETERS

RE = 0.4000E+07  MA =   0.450



SURGE POINT   -   CPeff = CPmax   KOCH(1981)

CX/Upro =   0.486   NUE =  0.468
CPmax =   0.441   L/G2  =  1.170
(I-Iref)r =   6.08   (I-Iref)s =    11.44


SURGE POINT  - (I-Iref)=(I-Iref)max

CX/Upro =  0.508   NUE =  0.000
CPmax =   0.417
(I-Iref)r =   4.86   DELBETAir =      7.09
(I-Iref)s =   9.17   DELBETAis =      9.18


CHOKE POINT

CX/Upro =  0.855   NUE =  0.926
(I-Iref)r =    -11.4   (I-Iref)s =     -20.9
MAr =  0.613   MAs =   0.464


OPTIMUM  POINT

CX/Upro =   0.607   ETA =  0.906   DCU =  0.293
NUE  =   0.633   MUEO =  0.394   MUEY =  0.357
REr  =  0.4899E+06   RECORr  =  0.894
REs  =  0.3531E+06   RECORs  =  0.944
MAr  =   0.545   CRMAr =   0.749   MACORr =  1.000
MAs  =   0.393   CRMAs =   0.715   MACORs =  1.000


CHARACTERISTIC  CURVE

CX/Up   CPR    OMGAr   OMGAs IIREFr IIREFs ETApro  BL     NUE   ETA      MUEO     MUEY
```

```
0.508 1.000 0.0207 0.0235   4.9   9.2  0.958  0.830  0.489  0.822  0.531  0.436
0.515 0.992 0.0200 0.0222   4.5   8.4  0.958  0.830  0.496  0.833  0.521  0.434
0.522 0.985 0.0193 0.0210   4.1   7.7  0.959  0.830  0.503  0.843  0.511  0.431
0.529 0.976 0.0187 0.0199   3.7   7.0  0.960  0.830  0.509  0.854  0.501  0.428
0.536 0.966 0.0181 0.0189   3.3   6.3  0.960  0.834  0.519  0.863  0.491  0.424
0.543 0.954 0.0176 0.0180   2.9   5.6  0.961  0.845  0.533  0.871  0.481  0.419
0.551 0.940 0.0172 0.0172   2.6   4.9  0.961  0.854  0.545  0.878  0.471  0.414
0.558 0.925 0.0168 0.0164   2.2   4.2  0.961  0.862  0.557  0.883  0.462  0.408
0.565 0.909 0.0164 0.0158   1.8   3.5  0.961  0.869  0.569  0.889  0.452  0.401
0.572 0.893 0.0161 0.0153   1.5   2.8  0.961  0.876  0.581  0.893  0.442  0.395
0.579 0.875 0.0158 0.0148   1.1   2.1  0.961  0.880  0.591  0.896  0.432  0.387
0.586 0.856 0.0156 0.0145   0.7   1.4  0.961  0.885  0.601  0.899  0.423  0.380
0.593 0.838 0.0154 0.0142   0.4   0.7  0.960  0.890  0.612  0.901  0.413  0.372
0.600 0.819 0.0153 0.0140   0.0   0.0  0.959  0.895  0.623  0.904  0.403  0.365
0.607 0.799 0.0154 0.0142  -0.4  -0.7  0.958  0.900  0.633  0.906  0.394  0.357
0.614 0.778 0.0156 0.0144  -0.7  -1.4  0.956  0.901  0.642  0.905  0.384  0.348
0.621 0.757 0.0158 0.0148  -1.1  -2.0  0.954  0.903  0.651  0.904  0.375  0.339
0.628 0.735 0.0160 0.0152  -1.4  -2.7  0.951  0.905  0.659  0.903  0.365  0.330
0.635 0.713 0.0163 0.0157  -1.8  -3.4  0.948  0.906  0.667  0.901  0.356  0.321
0.642 0.691 0.0166 0.0162  -2.1  -4.0  0.945  0.907  0.676  0.899  0.346  0.311
0.650 0.668 0.0170 0.0168  -2.5  -4.7  0.942  0.908  0.684  0.896  0.337  0.302
0.657 0.646 0.0174 0.0175  -2.8  -5.3  0.938  0.909  0.692  0.893  0.327  0.292
0.664 0.623 0.0178 0.0183  -3.1  -5.9  0.934  0.909  0.700  0.889  0.318  0.283
0.671 0.601 0.0183 0.0191  -3.5  -6.6  0.929  0.910  0.708  0.885  0.309  0.273
0.678 0.578 0.0188 0.0200  -3.8  -7.2  0.924  0.911  0.716  0.881  0.299  0.264
0.685 0.556 0.0194 0.0209  -4.1  -7.8  0.918  0.912  0.725  0.876  0.290  0.254
0.692 0.533 0.0199 0.0219  -4.5  -8.4  0.911  0.913  0.733  0.870  0.280  0.244
0.699 0.510 0.0206 0.0230  -4.8  -9.0  0.904  0.914  0.741  0.864  0.271  0.234
0.706 0.488 0.0212 0.0241  -5.1  -9.6  0.896  0.915  0.749  0.856  0.262  0.224
0.713 0.465 0.0219 0.0252  -5.5 -10.2  0.887  0.916  0.758  0.848  0.253  0.214
0.720 0.442 0.0226 0.0264  -5.8 -10.8  0.878  0.917  0.766  0.840  0.243  0.204
0.727 0.419 0.0234 0.0277  -6.1 -11.4  0.867  0.918  0.774  0.830  0.234  0.194
0.734 0.396 0.0242 0.0290  -6.4 -12.0  0.855  0.919  0.782  0.819  0.225  0.184
0.742 0.373 0.0250 0.0303  -6.7 -12.6  0.841  0.920  0.791  0.806  0.216  0.174
0.749 0.350 0.0258 0.0317  -7.0 -13.1  0.826  0.920  0.799  0.792  0.206  0.163
0.756 0.327 0.0267 0.0331  -7.3 -13.7  0.810  0.921  0.807  0.777  0.197  0.153
0.763 0.304 0.0277 0.0346  -7.6 -14.2  0.791  0.922  0.816  0.759  0.188  0.143
0.770 0.281 0.0286 0.0361  -8.0 -14.8  0.770  0.923  0.824  0.739  0.179  0.132
0.777 0.258 0.0296 0.0376  -8.3 -15.3  0.746  0.924  0.833  0.717  0.170  0.122
0.784 0.234 0.0306 0.0392  -8.6 -15.9  0.719  0.925  0.841  0.691  0.161  0.111
0.791 0.211 0.0317 0.0408  -8.9 -16.4  0.689  0.926  0.850  0.662  0.151  0.100
0.798 0.188 0.0328 0.0424  -9.1 -16.9  0.653  0.927  0.858  0.629  0.142  0.089
0.805 0.165 0.0339 0.0441  -9.4 -17.4  0.613  0.928  0.866  0.590  0.133  0.079
0.812 0.141 0.0351 0.0458  -9.7 -17.9  0.566  0.929  0.875  0.545  0.124  0.068
0.819 0.118 0.0363 0.0475 -10.0 -18.4  0.510  0.930  0.883  0.492  0.115  0.057
0.826 0.094 0.0375 0.0492 -10.3 -18.9  0.445  0.931  0.892  0.429  0.106  0.045
0.833 0.071 0.0388 0.0510 -10.6 -19.4  0.366  0.932  0.901  0.353  0.097  0.034
0.841 0.047 0.0401 0.0528 -10.9 -19.9  0.270  0.933  0.909  0.261  0.088  0.023
0.848 0.024 0.0414 0.0546 -11.2 -20.4  0.151  0.934  0.918  0.146  0.079  0.012
0.855 0.000 0.0428 0.0564 -11.4 -20.9  0.000  0.934  0.926  0.000  0.070  0.000
```

A.5.2 OUTPUT2.TXT

```
CX/Up    CNUE     CMUY     CETA     OMGAr    OMEGAs   CALFA1   CALFA2   CBETA1   CBETA2
0.508058 0.489049 0.436305 0.822288 0.020666 0.023452 14.6069  46.0430  59.6470  42.9593
0.515133 0.495859 0.433545 0.832748 0.019959 0.022164 14.5628  45.3191  59.2591  42.9242
0.522207 0.502669 0.430713 0.843378 0.019305 0.020974 14.5178  44.5979  58.8737  42.8886
```

0.529282	0.509479	0.427743	0.854100	0.018701	0.019879	14.4730	43.8790	58.4904	42.8532
0.536356	0.518740	0.423634	0.862884	0.018148	0.018879	14.4284	43.1627	58.1093	42.8179
0.543431	0.532746	0.419166	0.871229	0.017644	0.017975	14.3840	42.4492	57.7304	42.7829
0.550505	0.545286	0.413698	0.877747	0.017188	0.017164	14.3397	41.7388	57.3537	42.7481
0.557580	0.557104	0.407651	0.883233	0.016780	0.016445	14.2956	41.0315	56.9793	42.7135
0.564654	0.569144	0.401464	0.888591	0.016420	0.015819	14.2518	40.3278	56.6072	42.6791
0.571729	0.580527	0.394767	0.892980	0.016107	0.015283	14.2082	39.6276	56.2373	42.6450
0.578803	0.590752	0.387416	0.895998	0.015839	0.014837	14.1648	38.9313	55.8698	42.6110
0.585878	0.601080	0.379955	0.898836	0.015617	0.014478	14.1217	38.2390	55.5045	42.5773
0.592952	0.611695	0.372388	0.901499	0.015439	0.014206	14.0788	37.5509	55.1416	42.5437
0.600026	0.622518	0.364716	0.903972	0.015309	0.014020	14.0362	36.8672	54.7810	42.5104
0.607101	0.633485	0.356702	0.905641	0.015425	0.014193	13.9939	36.1880	54.4227	42.4773
0.614175	0.642123	0.347831	0.905106	0.015585	0.014445	13.9518	35.5136	54.0668	42.4444
0.621250	0.650793	0.338890	0.904304	0.015786	0.014775	13.9101	34.8439	53.7132	42.4117
0.628324	0.659162	0.329803	0.903001	0.016028	0.015181	13.8687	34.1793	53.3620	42.3793
0.635399	0.667408	0.320617	0.901296	0.016309	0.015660	13.8276	33.5198	53.0131	42.3470
0.642473	0.675607	0.311308	0.899085	0.016630	0.016211	13.7869	32.8655	52.6666	42.3150
0.649548	0.683729	0.301857	0.896271	0.016989	0.016832	13.7464	32.2165	52.3225	42.2832
0.656622	0.691867	0.292353	0.893074	0.017387	0.017521	13.7063	31.5731	51.9807	42.2516
0.663697	0.700022	0.282793	0.889458	0.017823	0.018275	13.6666	30.9352	51.6413	42.2203
0.670771	0.708191	0.273178	0.885385	0.018296	0.019093	13.6272	30.3029	51.3042	42.1891
0.677846	0.716377	0.263507	0.880811	0.018800	0.019973	13.5882	29.6764	50.9695	42.1582
0.684920	0.724579	0.253778	0.875686	0.019352	0.020912	13.5495	29.0558	50.6371	42.1275
0.691995	0.732797	0.243991	0.869954	0.019934	0.021909	13.5112	28.4410	50.3071	42.0970
0.699069	0.741030	0.234145	0.863557	0.020552	0.022961	13.4733	27.8322	49.9795	42.0667
0.706144	0.749280	0.224238	0.856407	0.021205	0.024066	13.4357	27.2294	49.6542	42.0367
0.713218	0.757546	0.214271	0.848435	0.021893	0.025223	13.3985	26.6326	49.3312	42.0068
0.720293	0.765827	0.204240	0.839541	0.022616	0.026429	13.3617	26.0420	49.0105	41.9772
0.727367	0.774125	0.194147	0.829612	0.023373	0.027683	13.3253	25.4575	48.6922	41.9478
0.734441	0.782438	0.183983	0.818521	0.024165	0.028982	13.2893	24.8792	48.3762	41.9186
0.741516	0.790768	0.173763	0.806116	0.024990	0.030325	13.2536	24.3072	48.0625	41.8896
0.748590	0.799114	0.163472	0.792218	0.025849	0.031710	13.2184	23.7413	47.7511	41.8608
0.755665	0.807476	0.153111	0.776618	0.026742	0.033134	13.1835	23.1816	47.4420	41.8322
0.762739	0.815854	0.142681	0.759062	0.027668	0.034597	13.1490	22.6282	47.1352	41.8039
0.769814	0.824249	0.132180	0.739248	0.028627	0.036097	13.1149	22.0811	46.8306	41.7757
0.776888	0.832660	0.121606	0.716807	0.029620	0.037632	13.0812	21.5402	46.5283	41.7478
0.783963	0.841087	0.110958	0.691289	0.030646	0.039200	13.0479	21.0055	46.2283	41.7201
0.791037	0.849530	0.100235	0.662133	0.031705	0.040800	13.0150	20.4770	45.9305	41.6926
0.798112	0.857990	0.089434	0.628637	0.032798	0.042430	12.9825	19.9548	45.6349	41.6652
0.805186	0.866467	0.078554	0.589909	0.033924	0.044090	12.9503	19.4387	45.3415	41.6381
0.812261	0.874960	0.067593	0.544794	0.035084	0.045777	12.9185	18.9288	45.0504	41.6112
0.819335	0.883470	0.056550	0.491779	0.036277	0.047491	12.8871	18.4251	44.7614	41.5845
0.826410	0.891996	0.045423	0.428833	0.037504	0.049231	12.8561	17.9275	44.4746	41.5580
0.833484	0.900540	0.034209	0.353167	0.038766	0.050994	12.8255	17.4359	44.1900	41.5317
0.840559	0.909100	0.022907	0.260854	0.040062	0.052781	12.7953	16.9504	43.9076	41.5056
0.847633	0.917678	0.011514	0.146165	0.041392	0.054590	12.7654	16.4709	43.6273	41.4797
0.854708	0.926273	0.000029	0.000426	0.042758	0.056421	12.7359	15.9973	43.3491	41.4540

Appendix B

Probabilistic Analysis Implementation

B.1 Overall View

Whereas the repeating-stage algorithm is set up as a Fortran 77 executable, the release 12 of MATLAB by developed by *The Mathworks* is used for the probabilistic analysis. This method allies the velocity of Fortran with the output possibilities of MATLAB. Figure B-1 illustrates the links between the MATLAB and Fortran modules.

Once the desired compressor and the coefficients for mean shift and variability are chosen, the algorithm runs as follows:

1. The VARIATION module reads the files describing the original compressor geometry `INPUTORI.TXT`, and the correlations determined by Garzon `CORR_IBR.TXT`. Variability is introduced to create the `INPUT.TXT` and `CORR.TXT` files, and they are processed by CHARAX. Results from individual runs in the `OUTPUT2.TXT` files are then gathered in the file `VARIATIONOUT.MAT`.

2. From `VARIATIONOUT.MAT`, the STAT module computes the mean value, the mean shift, the coefficient of variability and the skewness for the pressure rise and the efficiency. Results are put together in the `STAT.MAT` file.

3. From `STAT.MAT`, the DRAWGRAPH module draws graphs showing the variability introduced in the input and in the output.

4. The SETSTAT module gathers different `STAT.MAT` files to compare them.

All the steps mentioned above are detailed in the following sections.

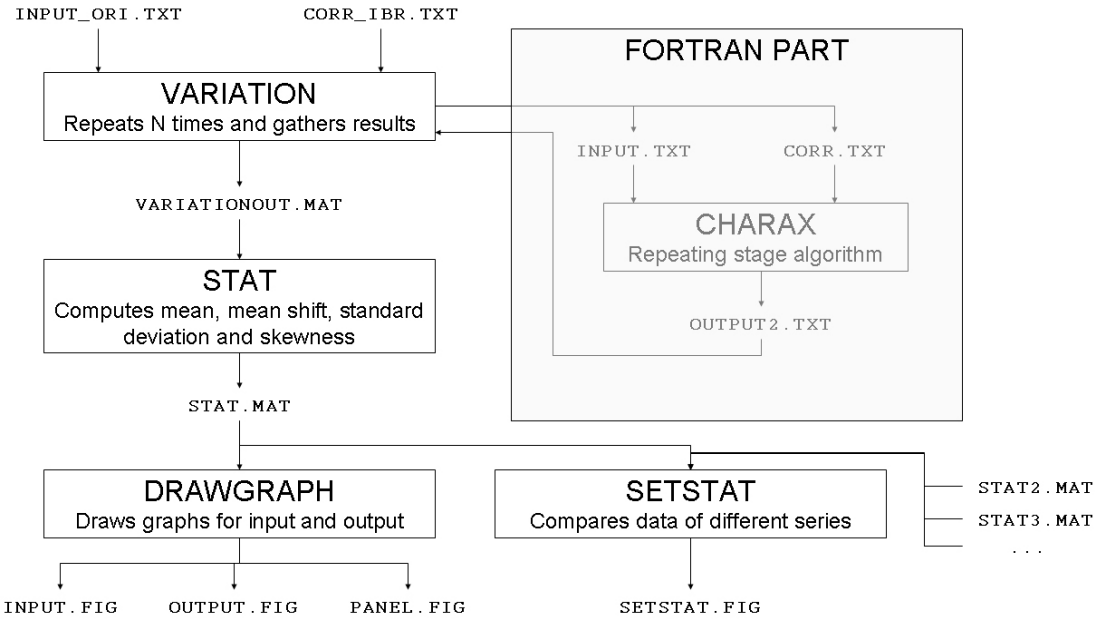

Figure B-1: Flow diagram for the probabilistic analysis

B.2 Monte Carlo Simulation

B.2.1 Introduction of Geometric Variability

The equations introducing geometric variability in the mean-line algorithm were presented in Section 4.2.1:

$$\frac{\epsilon_r}{h} = \left(\frac{\epsilon_r}{h}\right)_0 \cdot \left(1 + \Gamma_{\epsilon_r}^{\hat{V}} \cdot 50\% \cdot X_1\right) \tag{B.1}$$

$$\frac{\epsilon_s}{h} = \left(\frac{\epsilon_s}{h}\right)_0 \cdot \left(1 + \Gamma_{\epsilon_s}^{\hat{V}} \cdot 50\% \cdot X_2\right) \tag{B.2}$$

$$\vartheta(i_n) = \vartheta_0(i_n) \cdot \left(\Gamma_{\vartheta}^{\hat{S}} \cdot \hat{S}_{\vartheta}(i_n) + 1\right) \cdot \left(1 + \Gamma_{\vartheta}^{\hat{V}} \cdot \hat{V}_{\vartheta}(i_n) \cdot X_3\right) \tag{B.3}$$

$$\omega_r(i_n) = \omega_{r0}(i_n) \cdot \left(\Gamma_{\omega_r}^{\hat{S}} \cdot \hat{S}_{\omega_r}(i_n) + 1\right) \cdot \left(1 + \Gamma_{\omega_r}^{\hat{V}} \cdot \hat{V}_{\omega_r}(i_n) \cdot X_4\right) \tag{B.4}$$

$$\omega_s(i_n) = \omega_{s0}(i_n) \cdot \left(\Gamma_{\omega_s}^{\hat{S}} \cdot \hat{S}_{\omega_s}(i_n) + 1\right) \cdot \left(1 + \Gamma_{\omega_s}^{\hat{V}} \cdot \hat{V}_{\omega_s}(i_n) \cdot X_5\right), \tag{B.5}$$

where

$$X_1, X_2, X_3, X_4, X_5 \in \mathcal{N}(0,1).$$

The successive steps of the VARIATIONOUT module are:

1. It reads the `INPUT_ORI.TXT` and fixes the values for $\left(\frac{\epsilon_r}{h}\right)_0$ and $\left(\frac{\epsilon_s}{h}\right)_0$.
2. It reads the `CORR_IBR.TXT` and fixes the values for $\hat{S}_{\vartheta}(i_n)$, $\hat{S}_{\omega_r}(i_n)$, $\hat{S}_{\omega_s}(i_n)$, $\hat{V}_{\vartheta}(i_n)$, $\hat{V}_{\omega_r}(i_n)$, and $\hat{V}_{\omega_s}(i_n)$.
3. It conducts a baseline run to fix the relationship between ϕ_{pro} and i_n.

4. It reads user-defined values for the factors for mean shift and for coefficient of variability (usually $\Gamma^{\hat{S}} = \Gamma^{\hat{V}} = 1$).

5. It generates appropriate values for the random variables.

6. It computes the right hand side of Equations B.1 and B.2, and writes the `INPUT.TXT` file.

7. For Equations B.3, B.4 and B.5, the terms ϑ_0, ω_{r0} and ω_{s0} are not known in advance, so the remaining factors of the right hand side are stored as correlations in the `CORR.TXT` file, which looks as follows:

CXpro	WRcor	WScor	TURcor
0.478398	1.047093	0.985868	0.975086
0.523903	1.064864	0.980536	0.971703
0.554241	1.086667	0.973993	0.968886
0.569409	1.123741	0.985506	0.968074
0.584617	1.125052	0.967251	0.964172
0.588446	1.130233	0.965637	0.961450
0.592285	1.144626	0.959027	0.959716
0.596136	1.161283	0.971875	0.957759
0.600000	1.190156	0.981397	0.955451
0.603874	1.235403	1.024197	0.952902
0.607763	1.287726	1.079540	0.954807
0.611660	1.257393	1.090358	0.954768
0.615575	1.233787	1.082072	0.953980
0.631358	1.171042	1.060045	0.950534
0.680106	1.094752	1.033263	0.936200
0.731299	1.065525	1.023003	0.910170

8. It runs the CHARAX program with `INPUT.TXT` and `CORR.TXT` as inputs, and records the content of the `OUTPUT2.TXT` file in the `VARIATIONOUT.MAT` file.

9. It repeats steps 5, 6, 7 and 8 as many times as necessary to reach the number of requested runs.

The substitution between i_n and ϕ_{pro} can be noted. CHARAX carries out a linear interpolation to determine the value of the correction for each value of ϕ_{pro}, i.e. for each value of i_n.

B.2.2 Baseline Simulation

As can be noted in Section B.2.1, each Monte Carlo Simulation starts with a baseline run, where no variability is taken into account. The algorithm is run with $\Gamma^{\hat{S}} = \Gamma^{\hat{V}} = 0$. This baseline simulation has two reasons:

- It allows computing the mean shift, and thus comparing the impact of variability on performance.
- It fixes the relationship between ϕ_{pro} and i_n.

Indeed, the CHARAX algorithm uses the r.m.s. profile flow coefficient ϕ_{pro} as a reference parameter. In particular, the incidence angle $i_n = {\beta_1}^* - \beta_1$ is computed as a function of ϕ_{pro}. However, the correction factors for losses and turning due to geometric variability

are expressed in terms of turning angle. Therefore, it is convenient to fix once and for all the relationship between ϕ_{pro} and i_n. This relationship has to remain the same even when geometric variability is introduced, especially when it regards $\vartheta = \beta_1 - \beta_2$. For this reason, corrections brought to turning are implemented as pure deviation of β_2 while β_1 does not change.

B.2.3 Implementation of Variability in CHARAX

A study of the actual implementation of the variability in CHARAX helps in understanding the interdependence of variables mentioned in Table 4.1. As tip clearance variability is introduced in the `INPUT.TXT` file, it is fixed and cannot be influenced by any other variability. The deviation modifies the stalling static pressure rise, and therefore also the stage loading ratio. As a result, this deviation has an impact on ω_{r0}, ω_{s0} and ϑ_0, but the effect is negligible.

The profile losses ω_r and ω_s are actualized independently and are the last variables to be computed in the CURVE module, so that their final perturbation via Equations B.4 and B.5 has no effect on ϑ_0. The correction to turning is carried out ahead of the computation of the profile losses. As seen in Section B.2.2, only the β_2 angle is affected:

$$\beta_2 := \beta_1 - \vartheta_0 \cdot \left(\Gamma_\vartheta^{\hat{S}} \cdot \hat{S}_\vartheta(i_n) + 1\right) \cdot \left(1 + \Gamma_\vartheta^{\hat{V}} \cdot \hat{V}_\vartheta(i_n) \cdot X_3\right).$$

It can be seen in Section A.3.3 that this has a visible impact of ω_s, and none on ω_r. Therefore, Table 4.1 is now justified.

B.3 Statistics for All the Stages

Three sets of simulations are carried out:

1. A baseline simulation without perturbation to compare performance, and to determine the relationship between ϕ_{pro} and i_n;
2. A simulation with $\Gamma^{\hat{V}} = 0$ and $\Gamma^{\hat{S}} = 1$ to study the impact of the sole mean shift;
3. 2500 simulations with five random variables. The results of all these simulations are stored in the `VARIATIONOUT.MAT` file. The quantities recorded are based on those appearing in the `OUTPUT2.TXT` file as shown in Section A.5.2:
   (a) the hub flow coefficient ν
   (b) the pressure rise coefficient μ_y
   (c) the efficiency η
   (d) the r.m.s. two-dimensional flow coefficient ϕ_{pro}
   (e) the rotor losses ω_r
   (f) the stator losses ω_s
   (g) the relative inlet angle β_1
   (h) the relative outlet angle β_2
   (i) the incidence angle i_n

To facilitate the computation of ratios, the data are linearly interpolated so that all the values are expressed in terms of the incidence angle of the baseline case. Afterwards, for a given incidence angle, the mean value, the mean shift, the standard deviation and the skewness of the distribution in pressure rise and efficiency are computed. Results are stored in the `STAT.M` file.

Bibliography

[1] Casey, M. V., 1987. "A mean line prediction method for estimating the performance characteristic of an axial compressor stage." In *I. Mech. E. Conference 1987-6 Turbomachinery - Efficiency Prediction and Improvement*, Paper C 264/87. Cambridge.

[2] Casey, M. V., 1994. "Computational Methods for Preliminary Design and Geometry Definition in Turbomachinery." Number 195 in AGARD Lecture Series. NASA-Lewis.

[3] Crouse, J. E., 1974. "Computer Program for Definition of Transonic Axial-Flow Compressor Blade Rows." Technical report, NASA TN D-7345.

[4] Davis, W. R., 1970. "A computer program for the analysis and design of the flow in turbomachinery." Technical report, Ottawa, Carleton University report ME/A70-1.

[5] Drela, M. and Youngren, H., December 1998. *A User's Guide to MISES 2.53*. MIT Fluid Dynamic Research Laboratory, Cambridge MA 02139.

[6] Garzon, V. E., February 2003. *Probabilistic Aerothermal Design of Compressor Airfoils*. PhD dissertation, Massachusetts Institute of Technology.

[7] Garzon, V. E. and Darmofal, D. L., 2003. "Impact of Geometric Variability on Axial Compressor Performance." *ASME Jnl. of Turbomachinery*.

[8] Jansen, W. and Moffat, W. C., October 1967. "The Off-Design Analysis of Axial-Flow Compressors." *ASME Jnl. of Eng. for Power*, pages 453–462.

[9] Kerrebrock, J. L., 1992. *Aircraft Engines and Gas Turbines*. MIT Press, Cambridge, Massachusetts, second edition.

[10] Koch, C. C., October 1981. "Stalling Pressure Rise Capability of Axial Flow Compressor Stages." *ASME Jnl. of Eng. for Power*, 103:645–655.

[11] Koch, C. C. and Smith, L. H., Jr., 1976. "Loss Sources and Magnitudes in Axial Flow Compressors." *ASME Jnl. of Eng. for Power*, 98(3):411–424.

[12] Lavainne, J., September 2003. *Sensitivity of a Compressor Repeating-Stage to Geometric Variation*. Master's thesis, Massachusetts Institute of Technology.

[13] Lieblein, S., September 1959. "Loss and Stall Analysis of Compressor Cascades." *ASME Jnl. Basic Engineering*, pages 387–400.

[14] Lieblein, S., September 1960. "Incidence and Deviation angle correlation for compressor cascades." *Trans. ASME, Jnl. Basic Eng.*, pages 575–587.

[15] NUMECA International, June 2001. *Fine User Manual, Version 5.2*.

[16] Smith, L. H., Jr., 1970. "Casing Boundary Layers in Multistage Axial-Flow Compressors." *Flow Research on Blading*, 106:635–647.

[17] Trefethen, L. N. and Bau, D., 1997. *Numerical Linear Algebra*. Society for Industrial and Applied Mathematics, Philadelphia, PA.